BRNO UNIVERSITY OF TECHNOLOGY

VYSOKÉ UČENÍ TECHNICKÉ V BRNĚ

FACULTY OF MECHANICAL ENGINEERING

FAKULTA STROJNÍHO INŽENÝRSTVÍ

INSTITUTE OF PHYSICAL ENGINEERING

ÚSTAV FYZIKÁLNÍHO INŽENÝRSTVÍ

EXTERNAL BALLISTICS OF AIRGUN PROJECTILES

VNĚJŠÍ BALISTIKA PROJEKTILŮ PRO PLYNOVÉ ZBRANĚ

BACHELOR'S THESIS

BAKALÁŘSKÁ PRÁCE

AUTHOR   Tomáš Melichar

AUTOR PRÁCE

SUPERVISOR   doc. Ing. Stanislav Průša, Ph.D.

VEDOUCÍ PRÁCE

BRNO 2024

Assignment Bachelor's Thesis

Institut:	Institute of Physical Engineering
Student:	**Tomáš Melichar**
Degree programm:	Fundamentals of Mechanical Engineering
Branch:	Fundamentals of Mechanical Engineering
Supervisor:	**doc. Ing. Stanislav Průša, Ph.D.**
Academic year:	2023/24

As provided for by the Act No. 111/98 Coll. on higher education institutions and the BUT Study and Examination Regulations, the director of the Institute hereby assigns the following topic of Bachelor's Thesis:

External ballistics of airgun projectiles

Brief Description:

The number of airguns owned by public is constantly increasing. Manufacturers are reacting and new prototypes of airguns in wide range of calibers and power ratings are constantly coming to the market. Furthermore, the number of activities with airguns is experiencing the growth proportionally. Some of them require accurate estimation of projectile´s ballistic trajectory either due to neccesity of knowledge of the maximum range and the energy on impact, or simply due to importance of knowing the point of impact at longer ranges.

The mathematical solution of the projectile´s ballistic trajectory should be established on experimentally determined drag characteristic for the given projectile, generally known as drag function, in technical literature described as the drag law. The absence of the corresponding drag law or its substitution for an inadequate one results in non–negligable error when solving ballistics trajectories. This characteristic of the diabolo type airgun projectile is completely missing and is often replaced with the drag laws of differently shaped projectiles, for example with the drag law G1 and its derivative GA. Thus, we are consciously introducing a non–negligible error into the final ballistic trajectory solutions.

Bachelor's Thesis goals:

Reduction of the error in ballistics trajectories calculations of diabolo type small calibre airgun projectiles.

Recommended bibliography:

ŠAPIRO, Jakov Matvejevič. Vnější balistika. Praha: Státní nakladatelství technické literatury, 1953. Řada strojírenské literatury.

MCCOY, Robert. Modern exterior ballistics: the launch and flight dynamics of symmetric projectiles. Atglen, PA: Schiffer Publishing, 1999. ISBN: 0-7643-0720-7.

Deadline for submission Bachelor's Thesis is given by the Schedule of the Academic year 2023/24

In Brno,

L. S.

_____   _____

prof. RNDr. Tomáš Šikola, CSc.   doc. Ing. Jiří Hlinka, Ph.D.
Director of the Institute   FME dean

ABSTRACT

Throughout the paper, the reader is introduced to basic concepts and issues of exterior ballistics. Considering the problem stiffness, a suitable model of atmosphere is determined and combined with the optimal method of ballistic trajectories numerical modeling. Using PRODAS V3 software a basic aerodynamical characteristics of the small caliber reference projectile (diabolo type) model are estimated. Detailed attention is given to the description of the measurement platform, its errors, and optimization. Based on the experimental measurements of the given standard projectile, a new drag law JSBE is determined. The results between numerical solutions and real measurements are compared against measured drag law JSBE, G1/GA drag law, and software PRODAS V3 drag law estimation.

ABSTRAKT

V průběhu práce je čtenář seznámen se základními koncepty a problematikou vnější balistiky. Na základě náročnosti zvoleného modelu vnější balistiky je sestaven odpovídající model atmosférických podmínek společně s optimálním řešením pohybových diferenciálních rovnic numerickou integrací. Pomocí balistického softwaru PRODAS V3 jsou aproximovány základní aerodynamické charakteristiky referenčního malorážového projektilu typu diabolo. Důsledná pozornost je věnována popisu, vyhodnocení chyb a optimalizaci měřící platformy. Na základě experimentálních měření zvoleného referenčního projektilu je stanoven nový zákon odporu JSBE. Rozdíly mezi výsledky numerických řešení a reálných měření jsou následně porovnávány se stanoveným zákonem odporu JSBE, dále zákonem odporu G1/GA a aproximací zákonu odporu softwarem PRODAS V3.

KEY WORDS

airgun, GA, G1, drag function, drag law, diabolo, pellet, projectile

KLÍČOVÁ SLOVA

plynová zbraň, GA, G1, funkce odporu, zákon odporu, diabolo, diabolka, projektil

DECLARATION

I hereby declare that this bachelor's thesis was prepared as an original work by the author under the supervision of associate professor Ing. Stanislav Průša, PhD. I have listed all the literary sources, publications and other sources, which were used during the preparation of this thesis.

Tomáš Melichar

ACKNOWLEDGMENT

BIBLIOGRAPHIC CITATION

ROZŠÍŘENÝ ABSTRAKT

Práce je zaměřena na popis a zvýšení přesnosti výpočetních modelů vnější balistiky plynových zbraní. U plynových zbraní projektil získává kinetickou energii z expanze plynu, který byl předtím mechanicky stlačen. Plynem je myšlena jakékoliv látka nebo směs látek v plynném skupenství jako například vzduch, odtud se zbraně často nazývají jako vzduchové zbraně neboli vzduchovky (airguns). Konstrukce a operace plynových zbraní limituje maximální dosažitelnou hodnotu tlaku vzduchu a z tohoto důvodu vystřelené projektily nedosahují vysokých rychlostí. Střelivo určené do plynových zbraní je nejčastěji typu diabolo nazývaného také diabolka (pellet). Projektily typu diabolo se od ostatních odlišují především konstrukcí a způsobem stabilizace během letu.

Základním úkolem výpočetních modelů vnější balistiky je určení polohy a rychlosti projektilu v závislosti na čase. Trajektorie opisovaná projektilem po opuštění hlavně se nazývá balistickou křivkou, přičemž její tvar závisí na řadě faktorů. Uvažujeme-li pohyb projektilu v tíhovém poli a atmosférických podmínkách Země, jsou nejvýznamnějšími z nich odporová síla prostředí a působení gravitace. Ostatní dynamické veličiny způsobené pohybem projektilu kolem své osy nebo sklonem trajektorie zanedbáme (pohyb hmotného bodu). Směr tíhového zrychlení je vždy kolmý k teoretickému vodorovnému povrchu Země. Směr odporové síly je vždy opačný ke směru okamžitého pohybu projektilu. Známe-li směry působících sil a zrychlení, můžeme sestavit soustavu pohybových rovnic založených na Newtonově zákonu odporu a Newtonově druhém pohybovém zákonu. Kvůli povaze problému musí být rovnice v diferenciálním tvaru. Pro zvolený model plochých trajektorií je dostačující uvažovat projektil jako hmotný bod čímž se řešení redukuje na tři stupně volnosti (3DOF), odpovídající třem skupinám diferenciálních rovnic. Diferenciální rovnice lze řešit různými metodami numerické integrace, přičemž je vhodné zvolit kompromis odpovídající požadavkům na přesnost výpočtů a zároveň jejich náročnost. Numerická integrace má obvykle velmi vysoké množství iterací a je realizována pomocí softwarových algoritmů.

Zatímco velikost tíhového zrychlení považujeme za konstantní, odporová síla závisí především na relativní rychlosti projektilu vůči okolnímu vzduchu. Abychom určili její velikost, je zapotřebí definovat odporové parametry prostředí a aerodynamické vlastnosti daného projektilu. Zemská atmosféra je tvořená směsí plynů souhrnně nazývaných jako vzduch. Vlastnosti vzduchu lze popsat stavovou rovnicí ideálního plynu, s výjimkou příspěvku od vodní páry. Na základě této charakteristiky lze vzduch rozdělit na suchý a vlhký, přičemž popis vlastností vlhkého vzduchu je značně komplikovanější. Vlastnosti statické atmosféry jako ideálního plynu s absencí vodní páry (suchý vzduch) popisuje například model MSA (anglicky ISA – International Standard Atmosphere). Výstupem atmosférického modelu jsou údaje o hustotě vzduchu a rychlosti šíření zvuku v něm.

Protože řešíme soustavu se třemi stupni volnosti (3DOF) bude nás zajímat pouze jedna aerodynamická charakteristika, a to zákon odporu. Zákony odporu vychází z vlastností

součinitele odporu, který je definovaný jako součet dílčích součinitelů odporu pro daný aerodynamický jev (např.: součinitel vlnového odporu, tvaru, tření, …). Velikost dílčích koeficientů se mění v závislosti na relativní rychlosti projektilu vůči odporovému prostředí. Sečtením jednotlivých příspěvků obdržíme závislost koeficientu odporu na rychlosti projektilu. Ta se nazývá zákon odporu. Rychlost projektilu je vyjádřena v násobcích rychlosti zvuku, tedy Machově čísle. Zákony odporu vzduchu zahrnují do výpočtu pouze tvar projektilu a neumožňují tak porovnávat výsledné vlastnosti projektilů mezi sebou. Úplné charakteristiky je dosaženo pomocí balistického koeficientu, který kromě zákonu odporu zahrnuje do výpočtů i hmotnost a průměr daného projektilu.

Zákony odporu se odkazují na ilustrační výkres referenčního projektilu, pro který byl daný zákon naměřen, pro projektil typu diabolo však tento zákon neexistuje. Obvykle je nahrazován zákony odporu G1/GA, jejichž referenční projektil typu diabolo neodpovídá. Zákon odporu lze určit pomocí experimentálního měření aerodynamických vlastností daného projektilu. Nejdůležitější částí této práce je právě experimentální měření nového zákonu odporu JSBE odkazujícího se na referenční projektil JSB Exact v ráži 4.5 mm. Měřící aparatura je složena ze dvou sériově umístěných optických hradel Caldwell Precision Chronograph a je určena k měření úbytku rychlosti projektilu na definované vzdálenosti nazývané rozestup hradel. Uvažujeme-li odporovou sílu a zrychlení projektilu na této vzdálenosti konstantní, z pohybových rovnic lze zpětně vyjádřit závislost koeficientu odporu na rychlosti. K aproximaci aerodynamických charakteristik projektilu JSB Exact byl využit i software PRODAS, jehož primárním výstupem byl odhad zákonu odporu. Zákon odporu JSBE byl naměřen pro definované rychlostní spektrum omezené výkonem použitých plynových zbraní, zbylé části byly aproximovány na základě naměřených dat a odhadu softwaru PRODAS.

Porovnání přesnosti zákonů odporu je realizováno pomocí výpočtů poklesu rychlosti projektilu v závislosti na vzdálenosti balistickým softwarem. Veličiny vstupující do balistického softwaru byly vždy atmosférické podmínky, počáteční rychlost, hmotnost a balistické koeficienty projektilu odkazující se na zákony odporu JSBE, G1 a odhad softwaru PRODAS. Výsledky výpočtů byly následně porovnány se sadou radarových měření projektilu JSB Exact firmou JSB Match Diabolo. Zákon odporu JSBE dosáhl vyšší přesnosti pouze v určitém rozsahu počátečních rychlostí projektilu, cíle práce tedy bylo dosaženo pouze částečně.

CONTENTS

1 INTRODUCTION

Airguns, also known as air rifles, are operating on a principle of mechanically compressed gas, which is then simultaneously released accelerating the projectile down the barrel. The first mentions of this type of firearms comes from the 16th century. To this day, airguns are still popular among public as they are quiet, inexpensive and their ownership often does not require any license or permit. Together with the widespread usage grows a demand for a modern, more accurate and powerful airguns with increased range and lethality. Many of these airguns are used for pest control or sports shooting in a close vicinity to people and buildings which emphasizes the requirement of accurate estimation of projectile´s maximum range, its position at each point in flight and the energy on impact. These data are subsequently used to prevent unwanted injuries or damages to property.

Current external ballistics models cannot accurately describe the trajectory of the diabolo type projectile, due to the lack of aerodynamic characteristics of the projectile. External ballistic models must be established on experimentally determined drag characteristic for the given projectile, based on the projectile shape, aerodynamic behavior and other properties. The basic aerodynamic characteristic is known as drag function, in technical literature described as the drag law. The drag law of the diabolo type projectile has not yet been determined; therefore, it is substituted with the drag law of other similar projectiles, resulting in non-negligible error in computed trajectories.

This work focuses on the description and improvement of the external ballistic model of diabolo type projectile trajectories. The first two chapters serve as a theoretical basis, describing the effect of atmospheric conditions and external forces acting on the projectile in flight. The reader is also introduced to the numerical solution used in the developed B4E ballistic solver [9]. The rest of the work is dedicated to measuring, processing and evaluation of the resulting aerodynamical characteristics of the diabolo type projectile. The resulting model was then compared to the current model and subsequently implemented in the B4E open-source ballistic solver available to the public.

2 ATMOSPHERE

Most problems related to exterior ballistics arise in the Earth's atmosphere. The trajectory of a projectile is influenced by various aerodynamic forces and rapidly changing winds. The atmosphere is a layer of gravitationally attracted gases, known collectively as air. It is mainly composed of nitrogen $N_2(\sim78\%)$, oxygen $O_2(\sim21\%)$ and other gases of which Argon Ar ($\sim0.9\%$) and water vapor H_2O ($up\ to\ \sim3\%$) are the two most abundant. The key objective of this chapter is to determine the density of air and the speed of sound. The properties of air vary significantly with increasing altitude. To characterize the relationship between temperature, pressure and altitude various mathematical models had been established. I will use the International Standard Atmosphere (ISA) model. ISA can be described as a static atmospheric model with fixed air properties at given altitudes. It also considers air as a fully compressible ideal gas. Although not comparable with recent global atmospheric models, the ISA is often used by many for ballistics or aviation computations with sufficient accuracy, while not requiring hard-to-obtain data. Depending on altitude the ISA atmosphere is divided into six segments. From sea level to Kármán line, defining an imaginary boundary between atmosphere and outer space.

Layer	Name	Average altitude [km]
1	Troposphere	$0 - 11$
2	Tropopause	$11 - 20$
3	Stratosphere	$20 - 47$
4	Stratopause	$47 - 51$
5	Mesosphere	$51 - 85$
6	Mesopause	$85 - 100$

Table 1: Atmospheric layers distribution with altitude.

The Table 1 and Figure 1 considers average layer height, which varies with latitude. For example, at the poles the Troposphere ends at mere 6 km above sea level, while at the equator it can as well reach 18 km. Each atmosphere layer has its own temperature vs altitude linear distribution. Pressure and density decrease with altitude at exponential rates. One would expect the temperature in lower atmospheric layers to steadily decrease with increasing altitude. Despite that, the temperature in stratosphere rapidly increases due to high concentration of ozone. Production of ozone generates heat, increasing the air temperature. Additionally, ozone is a greenhouse gas and can retain heat. Small arms projectiles cannot reach out of the Troposphere even when fired perpendicularly to the ground, therefore defining the Troposphere is our only concern.
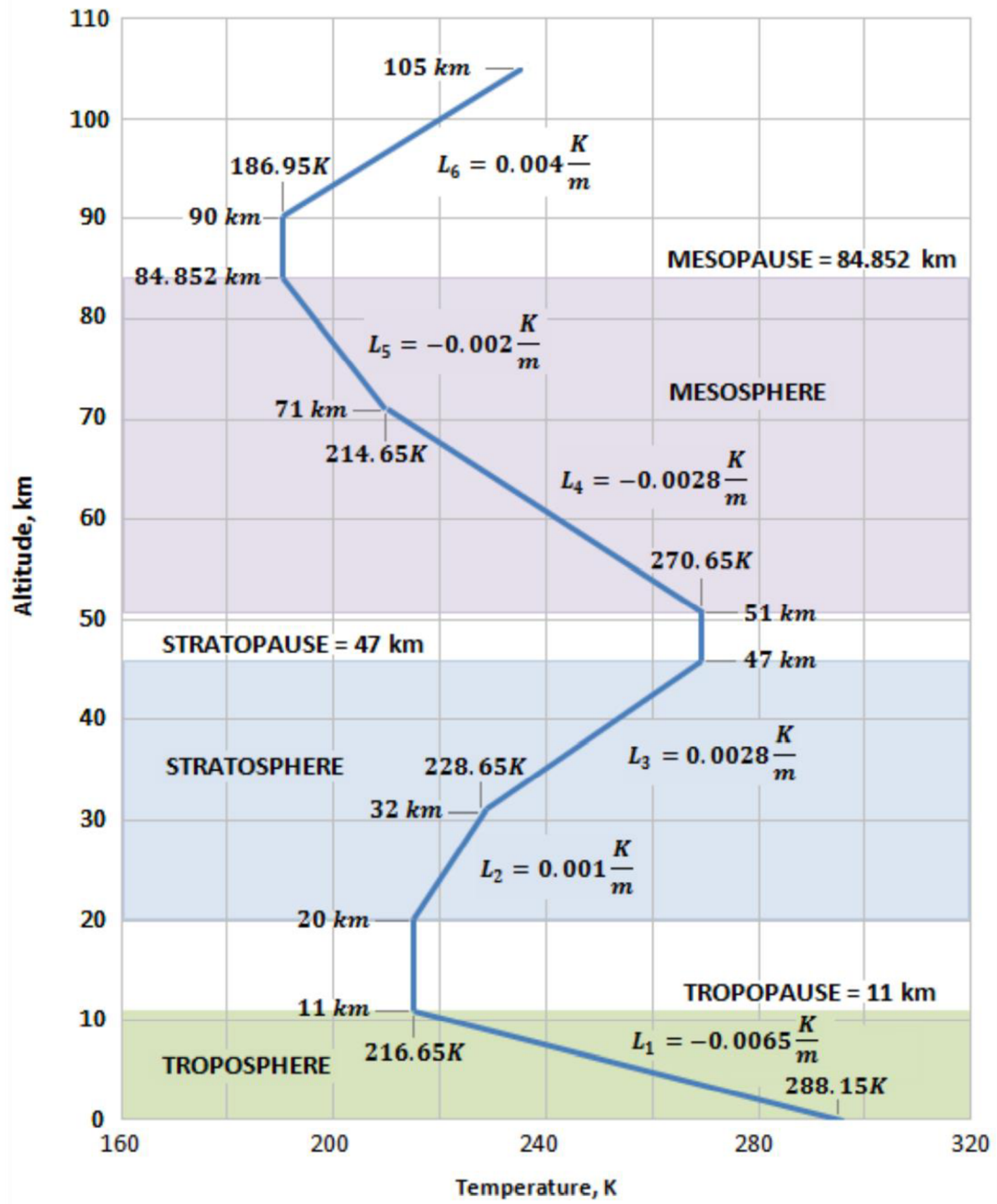
Figure 1: Air temperature variation with altitude according to the International Standard Atmosphere (ISA) model. Adapted from: [1].

2.1 Definition of fundamental variables

p [Pa] – Absolute air pressure

p_{da} [Pa] – Partial pressure of dry air

p_{wv} [Pa] – Partial pressure of water vapor

p_{wvs} [Pa] – Partial pressure of saturated water vapor

r [J $\cdot$ kg^{-1} $\cdot$ K^{-1}] – Specific gas constant

$r_{da} = 287.050$ [J $\cdot$ kg^{-1} $\cdot$ K^{-1}] – Specific gas constant of dry air

$r_{wv} = 461.495$ [J $\cdot$ kg^{-1} $\cdot$ K^{-1}] – Specific gas constant of water vapor

v [m^3 $\cdot$ kg^{-1}]; v [m $\cdot$ s^{-1}] – Specific air volume; Velocity of an object relative to air

ρ [kg $\cdot$ m^{-3}] – Air density

ρ_{da} [kg $\cdot$ m^{-3}] – Density of dry air

ρ_{wv} [kg $\cdot$ m^{-3}] – Density of water vapor

φ [%] – Relative air humidity

T [K] – Absolute air temperature

T_C [°C] – Relative air temperature

h [m] – Altitude (Height above sea level)

c [m $\cdot$ s^{-1}] – Speed of sound

c_{da} [m $\cdot$ s^{-1}] – Speed of sound in dry air

γ [−] – Poisson´s constant (For dry air $\gamma = 1.4$)

K [MPa] – Bulk modulus of liquid

2.2 Density of dry air

Using the ISA static atmospheric model (Figure 1), we can compute the density in three ways, depending on the available data. In first and the best-case scenario we know the exact air

pressure and temperature. In the second, the most common case, we know the exact temperature and altitude. Finally, in the third case, we only know the altitude.

Neglecting the effect of water vapor, the water vapor partial pressure p_{wv} must be equal to zero. That means any of the computed variables of dry air is equal to its absolute value in air.

$$p = p_{da} \qquad (1)$$

$$\rho = \rho_{da} \qquad (2)$$

The ISA considers the air as an ideal fully compressible gas, so it can be solved using the standard equation of state. The equation is written using the specific volume and specific gas constant:

$$p \cdot v = r \cdot T. \qquad (3)$$

By expressing the air density from the standard equation of state, we get the equation for first case scenario problem computation:

$$\rho_{da} = \frac{1}{v} = \frac{p_{da}}{r_{da} \cdot T} \ [\text{kg} \cdot \text{m}^{-3}]. \qquad (4)$$

For the second case scenario computation we need to combine the equation of state with a pressure altitude equation *(10)* to determine atmospheric pressure at a given altitude. Expecting the air pressure, density and temperature in Troposphere to decline at a known rate, first, we must define initial conditions bound to zero altitude (sea level):

$p_0 = 101325 \ \text{Pa}$,

$\rho_0 = 1.225 \ \text{kg} \cdot \text{m}^{-3}$,

$T_0 = 288.15 \ \text{K}$.

To derive the pressure altitude equation, we must consider some quantities as constant. First, we need to separate the pressure from the standard equation of state *(3)*, getting the Barometric formula:

$$p = \frac{1}{v} \cdot r \cdot T = \rho \cdot r \cdot T. \qquad (5)$$

If atmospheric pressure comes from the hydrostatic pressure, we can use the hydrostatic equation for ideal fluid:

$$\mathrm{d}p = -\rho \cdot g \cdot \mathrm{d}h. \qquad (6)$$

Dividing the hydrostatic equation *(6)* by the Barometric formula *(5)* and then integrating this equation between altitudes $h_0 = 0$ m (sea level) and h:

$$\frac{dp}{p} = -\frac{g \cdot dh}{r \cdot T},$$

(7)

$$\int_{p_0}^{p} \frac{dp}{p} = -\frac{g}{r \cdot T} \cdot \int_{h_0}^{h} dh.$$

(8)

With all integration steps completed, we can implement the ISA equation of linear temperature decrease in Troposphere ($T = T_0 - 0.0065 \cdot h$) [1]. Additionally, if we consider that the gravitational acceleration in Troposphere has a constant value of $g = 9.81$ m $\cdot$ s^{-2} and knowing the specific gas constant of dry air, we can substitute both into the equation and simplify:

$$p = p_0 \cdot \left(\frac{T}{T_0}\right)^{\frac{g}{r \cdot 0.0065}} = p_0 \cdot \left(1 - \frac{0.0065 \cdot h}{T_0}\right)^{5.2577}.$$

(9)

Since all previous computation steps are based on the given initial temperature T_0 and pressure p_0, we can also substitute their exact value getting a final form of pressure altitude equation for our second case scenario computation:

$$p = 101325 \cdot \left(1 - \frac{h}{44331}\right)^{5.2577} \text{ [Pa]}.$$

(10)

Using similar process, we can derive the relationship between altitude and density for the third case scenario computation:

$$\rho = \rho_0 \cdot \left(1 - \frac{0.0065 \cdot h}{T_0}\right)^{4.2577} = 1.225 \cdot \left(1 - \frac{h}{44331}\right)^{4.2577} \text{ [kg} \cdot \text{m}^{-3}\text{]}.$$

(11)

To determine accuracy of the ISA modified model we will select six random atmospheric data measurements from two RBCN stations in Czechia, operated by Czech hydrometeorological institute ČHMÚ. All measured data represents an average daily variable value. To test the model on wider range of temperatures and altitudes, each selected measurement is taken in a different season and at different altitude. Since ČHMÚ datasheet does not contain any air density data, the error of the computation scenarios will be compared against the first case scenario (theoretically most dependable).

Data from the RBCN meteorological station in Přibyslav [2]:

Date [−]	Altitude above sea level [m]	Average air temperature [°C]	Average air pressure [hPa]	Relative humidity [%]	Wind speed [m · s⁻¹]	Total rainfall [mm]
11.01.2022	532.5	-7.1	967.9	92	2.9	0
04.08.2022	532.5	24.6	955.5	41	3.4	0
07.10.2022	532.5	12.6	961.8	87	4.6	0

Table 2: Data from the RBCN meteorological station located in Přibyslav (Czechia). Data available from: [2].

Case [−]	Altitude [m]	Air temperature [°C]	Air pressure [hPa]	Air density [kg · m⁻³]	Proportional deviation from Case 1 [%]
1	532.5	-7.1	967.9	**1.2674**	-
1	532.5	24.6	955.5	**1.1179**	-
1	532.5	12.6	961.8	**1.1726**	-
2	532.5	-7.1	950.9	**1.2451**	-1.8
2	532.5	24.6	950.9	**1.1126**	-0.5
2	532.5	12.6	950.9	**1.1593**	-1.2
3	532.5	-	-	**1.1636**	-8.9
3	532.5	-	-	**1.1636**	3.9
3	532.5	-	-	**1.1636**	-0.8

Table 3: Computed values of air pressure and air density for each case from the Table 2 using equations (4), (10), (11).

Data from the RBCN meteorological station at Lysá Hora mountain [2]:

Date [−]	Altitude above sea level [m]	Average air temperature [°C]	Average air pressure [hPa]	Relative humidity [%]	Wind speed [m · s⁻¹]	Total rainfall [mm]
11.01.2022	1322	-10.8	873.2	99	7.5	0
04.08.2022	1322	18.5	872.9	59	2.8	0
07.10.2022	1322	9.9	876.3	83	6.3	0

Table 4: Data from the RBCN meteorological station located at Lysá Hora mountain (Czechia). Data available from: [2].

Case [−]	Altitude [m]	Air temperature [°C]	Air pressure [hPa]	Air density [kg · m⁻³]	Proportional deviation from Case 1 [%]
1	1322	-10.8	873.2	**1.1595**	-
1	1322	18.5	872.9	**1.0427**	-
1	1322	9.9	876.3	**1.0785**	-
2	1322	-10.8	864.2	**1.1476**	-1.0
2	1322	18.5	864.2	**1.0323**	-1.0
2	1322	9.9	864.2	**1.0636**	-1.4
3	1322	-	-	**1.0769**	-7.7
3	1322	-	-	**1.0769**	3.2
3	1322	-	-	**1.0769**	-0.1

Table 5: Computed values of air pressure and air density for each case from the Table 4 using equations (4), (10), (11).

Summarizing all the computed data, we can conclude that the second case scenario is clearly more accurate than the third, especially at evaluating air density during temperature deviations. Although the second case scenario does not always give accurate atmospheric pressure value, we can say that in most cases the error of air density computation should be within 2 % of the first case scenario. Note that both models usually predict a lower air density value than the first case scenario.

2.3   Density of humid air

Humid air can be considered as an extension of dry air accounting for the dispersed water vapor rather than separate model, creating somewhat more realistic model of atmospheric conditions.

The ISA doesn't account for water vapor presence. Computation of water vapor partial density requires the partial pressure of dry air and the overall air temperature. Since the dry air pressure computation is based on ISA static atmosphere model, the estimation of humid air density can only be as good as the ISA estimation is.

Accounting for water vapor, the final pressure becomes a sum of partial dry air pressure and partial water vapor pressure. The same is true for air density.

$$p = p_{da} + p_{wv} \tag{12}$$

$$\rho = \rho_{da} + \rho_{wv} \tag{13}$$

Expressing the water vapor density from equation of state (3), we get:

$$\rho_{wv} = \frac{p_{wv}}{r_{wv} \cdot T} \ [\mathrm{kg} \cdot \mathrm{m}^{-3}]. \tag{14}$$

Substituting all the variables we obtain the equation for computing density of humid air:

$$\rho = \frac{p_{da}}{r_{da} \cdot T} + \frac{p_{wv}}{r_{wv} \cdot T} \ [\mathrm{kg} \cdot \mathrm{m}^{-3}]. \tag{15}$$

Now we are left with one unknown variable – partial water vapor pressure. Water vapor is not an ideal gas, meaning its properties are determined by experimental measurements. The saturation pressure of water vapor is dependent on the humid air temperature. Water vapor saturation pressure represents water vapor pressure at relative humidity $\varphi = 100$ %.

Using the Arden Buck equation for computation of saturated water vapor pressure [3]:

$$p_{wvs} = 0.61121 \cdot \exp\left[\left(18.678 - \frac{T_C}{234.5}\right) \cdot \left(\frac{T_C}{257.14 + T_C}\right)\right] \ [\mathrm{kPa}]. \tag{16}$$

The relative humidity can be written as the ratio of partial water vapor pressure and saturated water vapor pressure:

$$\varphi = \frac{p_{wv}}{p_{wvs}} \cdot 100 \ [\%]. \tag{17}$$

We can substitute the saturated water vapor pressure into the Arden Buck equation (16) obtaining the final form of equation for partial water vapor pressure computation dependent on the saturated water vapor pressure and temperature:

$$p_{wv} = 6.1121 \cdot \varphi \cdot \exp\left[\left(18.678 - \frac{T_C}{234.5}\right) \cdot \left(\frac{T_C}{257.14 + T_C}\right)\right] \ [\mathrm{Pa}]. \tag{18}$$

Note that this form of Arden Buck equation cannot be used for temperatures $T_C \leq 0$ °C, when the water in the air can exist in all three states – water vapor, ice crystals and water drops.

Except of precise ballistics computations (trajectories of long-range artillery shells and such) partial density of water vapor is often neglected for its little or no effect on the air density. To test this hypothesis let´s consider the following atmospheric conditions to achieve maximum effect of water vapor pressure: $T_C = 40\,°\text{C}$, $h = 500$ m, $\varphi = 100\,\%$.

Solving for partial dry air and water vapor pressure:

$$p_{da} = 101325 \cdot \left(1 - \frac{h}{44331}\right)^{5.2577} = 101325 \cdot \left(1 - \frac{500}{44331}\right)^{5.2577} = 95459 \text{ Pa,}$$

$$p_{wv} = 6.1121 \cdot 100 \cdot exp\left[\left(18.678 - \frac{40}{234.5}\right) \cdot \left(\frac{40}{257.14 + 40}\right)\right] = 7382 \text{ Pa.}$$

Solving for the partial dry air and water vapor density and the final air density:

$$\rho_{da} = \frac{p_{da}}{r_{da} \cdot T} = \frac{95459}{287.05 \cdot 313.15} = 1.062 \text{ kg} \cdot \text{m}^{-3},$$

$$\rho_{wv} = \frac{p_{wv}}{r_{wv} \cdot T} = \frac{7382}{461.495 \cdot 313.15} = 0.051 \text{ kg} \cdot \text{m}^{-3},$$

$$\rho = \rho_{da} + \rho_{wv} = 1.0620 + 0.0511 = 1.113 \text{ kg} \cdot \text{m}^{-3}.$$

Neglecting the partial density of water vapor is, under given circumstances, justifiable. Water vapor density in this extreme case made up just 4.59 % of the total density. Furthermore, we can say that in majority of cases the water vapor density will not exceed 2 % of the total air density.

2.4   Speed of sound

Speed of sound as a quantity and sound barrier as an aerodynamic phenomenon is the subject of research not only in ballistics. It also serves as a basis for majority of characteristics including drag laws. The exact value of speed of sound is often referred to as Mach number [Ma] – a dimensionless ratio of an object velocity compared to the speed of sound $v_{Ma} = v/c$. Unlike air density, the speed of sound is relatively easy to approximate and is independent of changes in air pressure and humidity. Sound can be defined as a pressure wave which propagates through a given liquid at velocity, described by the Newton–Laplace equation [4]:

$$c = \sqrt{\frac{K}{\rho}}.$$

(19)

Assuming dry air as an ideal gas, we can express the Bulk modulus of liquid as follows:

$$K = \gamma \cdot p. \qquad (20)$$

Substituting dry air pressure into the Newton–Laplace equation *(19)* using the standard equation of state *(3)*, we get the final relation of the speed of sound and dry air temperature:

$$p = \rho \cdot r_{da} \cdot T, \qquad (21)$$

$$c_{da} = \sqrt{\frac{\gamma \cdot p}{\rho}} = \sqrt{\gamma \cdot r_{da} \cdot T}. \qquad (22)$$

Since the γ and r_{da} are both constants and since the temperature is often measured in degrees Celsius, we may encounter additional form of the same equation based on linear function approximation [4]:

$$c_{da} \approx 331.3 + 0.6 \cdot T_C \ [\mathrm{m} \cdot \mathrm{s}^{-1}]. \qquad (23)$$
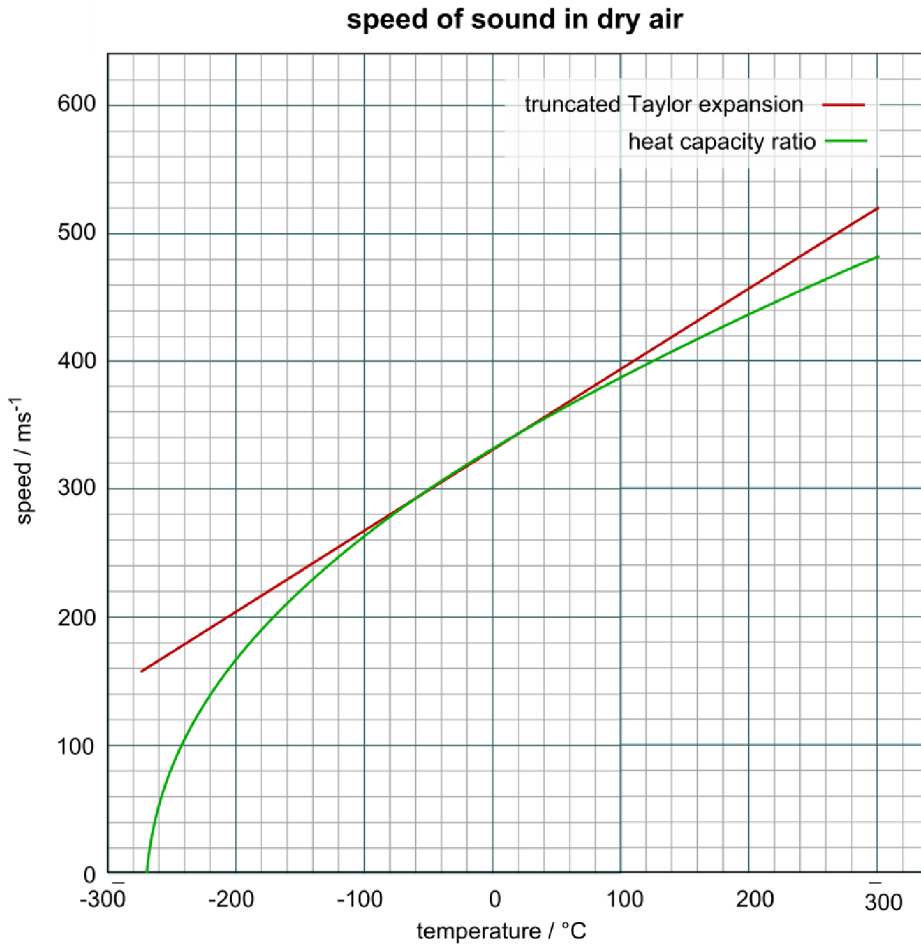
Figure 2: Approximation of the speed of sound in dry air based on the heat capacity ratio (in green) against the truncated Taylor expansion (in red, described by equation *(23)*). Available at: [4].
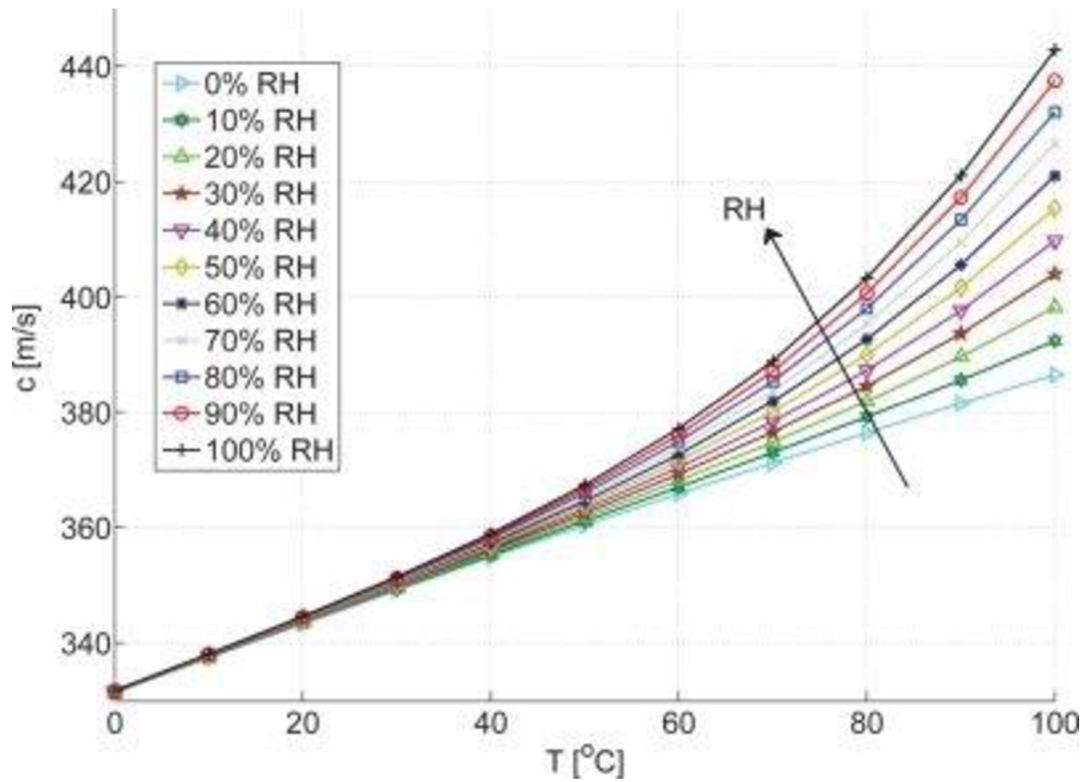
Figure 3: Speed of sound vs. temperature and relative humidity, p = 101.3 kPa, 314 ppm CO_2.
Available at: [5].

Once again, measurements and more complex approximations gives us the knowledge of boundaries within which the linear approximation can be used. According to the data displayed in the Figure 2 and Figure 3, we will set the computation limits of temperature T_C from $T_{Cmin} = -40\,°C$ to $T_{Cmax} = 40\,°C$.

3 MATHEMATICAL DESCRIPTION OF EXTERNAL BALLISTICS

3.1 Definition of fundamental variables

ρ [kg·m^{-3}] – Air density

S [m^2] – Cross-sectional area of the projectile

SD [lb·in^{-2}, kg·m^{-2}] – Sectional density of the projectile

m [kg] – Weight of the projectile

C_x [−] – Drag coefficient

C_s [−] – Drag coefficient of the drag law reference projectile

i [−] – Form factor

BC [lb·in^{-2}, kg·m^{-2}] – Ballistic coefficient

g [m·s^{-2}] – Gravitational acceleration

d [m] – Diameter of the projectile

v [m·s^{-1}] – Velocity of the projectile

$v_{x,y,z}$ [m·s^{-1}] – Axial components of projectile´s velocity

a [m·s^{-2}] – Acceleration of the projectile

$a_{x,y,z}$ [m·s^{-2}] – Axial components of projectile´s acceleration

x, y, z [m] – Axial components of projectile´s position from origin

t [s] – Time of projectile movement

h [s] – Time step of numerical integration

k [NaN] – Column of numerical integration

3.2 Differential equations

The purpose of differential equations is to describe the change in defined system over time. Forming the core of each ballistic solver, differential equations of motion are solved using

15

numerical integration with a given time step. The time step can be preset or changed based on the input data throughout the computation process.

Airguns are handheld shoulder fired firearms. Similarly, to most handheld firearms we can characterize the projectile trajectory as flat. Doing so, the atmospheric density does not change with altitude, and we consider the projectile as a point mass, reducing the solution to 3DOF (Three Degrees of Freedom – axes x, y, z). The solution is partially derived from the Newton´s second law of motion and drag equations (37), (48), (49). For 3DOF point mass solution we can write the following system of second order differential equations:

$$\frac{\mathrm{d}v}{\mathrm{d}t} = \frac{C_x \cdot \rho \cdot S \cdot v^2}{2 \cdot m},$$

$$\frac{\mathrm{d}v_y}{\mathrm{d}t} = \frac{\mathrm{d}v}{\mathrm{d}t} \cdot \frac{v_y}{v} + g,$$

$$\frac{\mathrm{d}v_x}{\mathrm{d}t} = \frac{\mathrm{d}v}{\mathrm{d}t} \cdot \frac{v_x}{v},$$

$$\frac{\mathrm{d}v_z}{\mathrm{d}t} = a_z,$$

$$\frac{\mathrm{d}y}{\mathrm{d}t} = v_y,$$

$$\frac{\mathrm{d}x}{\mathrm{d}t} = v_x,$$

$$\frac{\mathrm{d}z}{\mathrm{d}t} = v_z.$$

(24)

Notice that the solution could be written using just four differential equations instead of five. The velocities form a right triangle, and we can use the Pythagorean theorem to describe them:

$$v^2 = v_x^2 + v_y^2 + v_z^2.$$

(25)

Now that we have the relevant flat trajectory model described, we need to choose an appropriate method of numerical integration. Due to the relatively low difficulty of the 3DOF model, we will choose from a few common integration methods used to solve ordinary differential equations. Generally characterizing the initial problem, we introduce an unknown variable y, whose magnitude is changing over time. The value of y at $t_0 = 0 \, \mathrm{s}$ is initial value marked as y_0:

$$y(t_0) = y_0.$$

(26)

The change of variable y over time depends on the value of y at the beginning of each integration step:

$$\frac{dy}{dt} = f(t, y).$$

<div align="right">(27)</div>

This equation further underlines the importance of using numerical integration method as the change of defined variable depends on itself. The last undescribed variables are: h, representing a constant time interval also called time step and k, representing result obtained by single integration also called integration column. The time step h can be set as desired but it is important to do an analysis of the algorithm accuracy as an incorrectly set time step may cause degradation in accuracy or increase in computation time.

Fourth order Runge–Kutta integration method (RK4) [6]:

$$k_1 = h \cdot f(t_n, y_n),$$

$$k_2 = h \cdot f\left(t_n + \frac{h}{2}, y_n + \frac{k_1}{2}\right),$$

$$k_3 = h \cdot f\left(t_n + \frac{h}{2}, y_n + \frac{k_2}{2}\right),$$

$$k_4 = h \cdot f(t_n + h, y_n + k_3),$$

$$y_{n+1} = y_n + \frac{1}{6} \cdot (k_1 + 2 \cdot k_2 + 2 \cdot k_3 + k_4),$$

$$t_{n+1} = t_n + h.$$

<div align="right">(28)</div>

Second order Runge–Kutta integration method (RK2) [6]:

$$k_1 = h \cdot f(t_n, y_n),$$

$$k_2 = h \cdot f(t_n + h, y_n + k_1),$$

$$y_{n+1} = y_n + \frac{1}{2} \cdot (k_1 + k_2),$$

$$t_{n+1} = t_n + h.$$

<div align="right">(29)</div>

Euler integration method [6]:

$$k = h \cdot f(t_n, y_n),$$

$$y_{n+1} = y_n + k,$$

<div align="right">(30)</div>

$$t_{n+1} = t_n + h.$$

In general, we want all algorithms to be as accurate as needed and as fast as possible. Translated into our problem we want to find the optimal combination of the integration method and time step. To do so all integration methods were programmed in software MATLAB R2022b. The total duration of each computation process was measured, and the resulting trajectory compared against the MATLAB numerical integration function ODE45 in terms of maximum projectile range. The results are displayed in Figure 4.

Based on the plotted data we can conclude that the RK2 with step size of $h = 10^{-3}$ s is the optimal method for the flat trajectory 3DOF model as it achieved nearly similar results as RK4. Nevertheless, the RK4 method is still great option for solving difficult differential equations but implementing it for this solution does not yield any advantages. Euler method on the other hand is the simplest and fastest method of numerical integration but has a big disadvantage of error accumulation and inaccuracy.
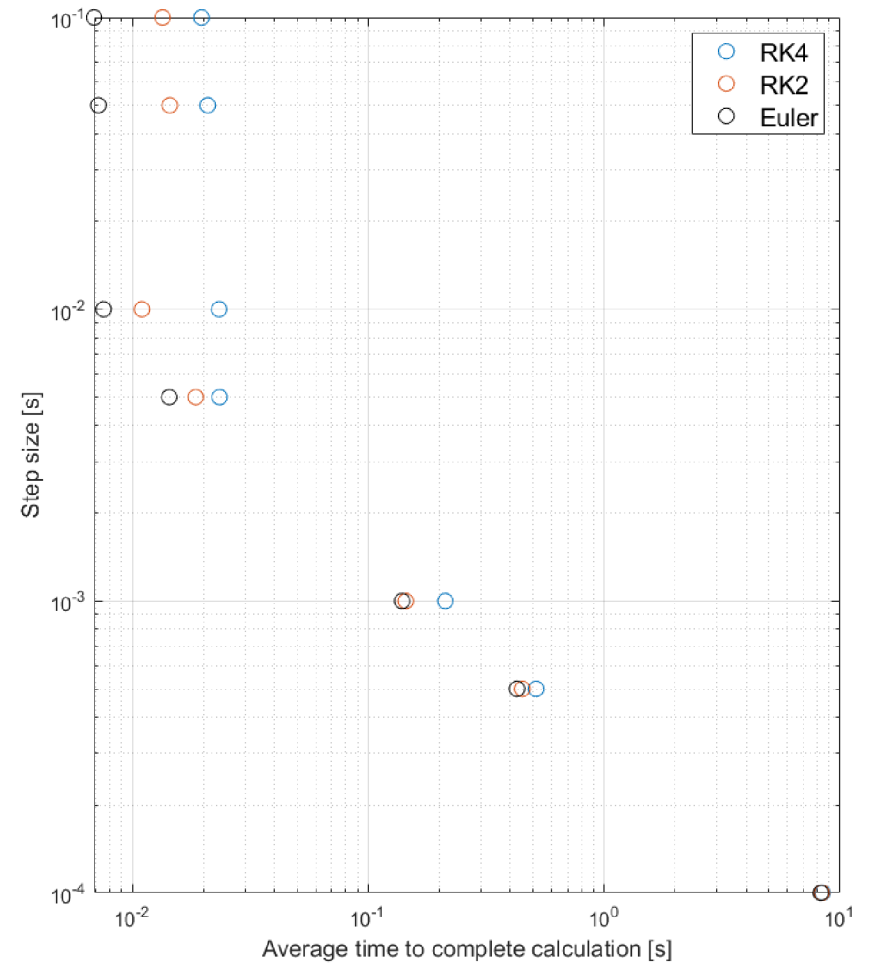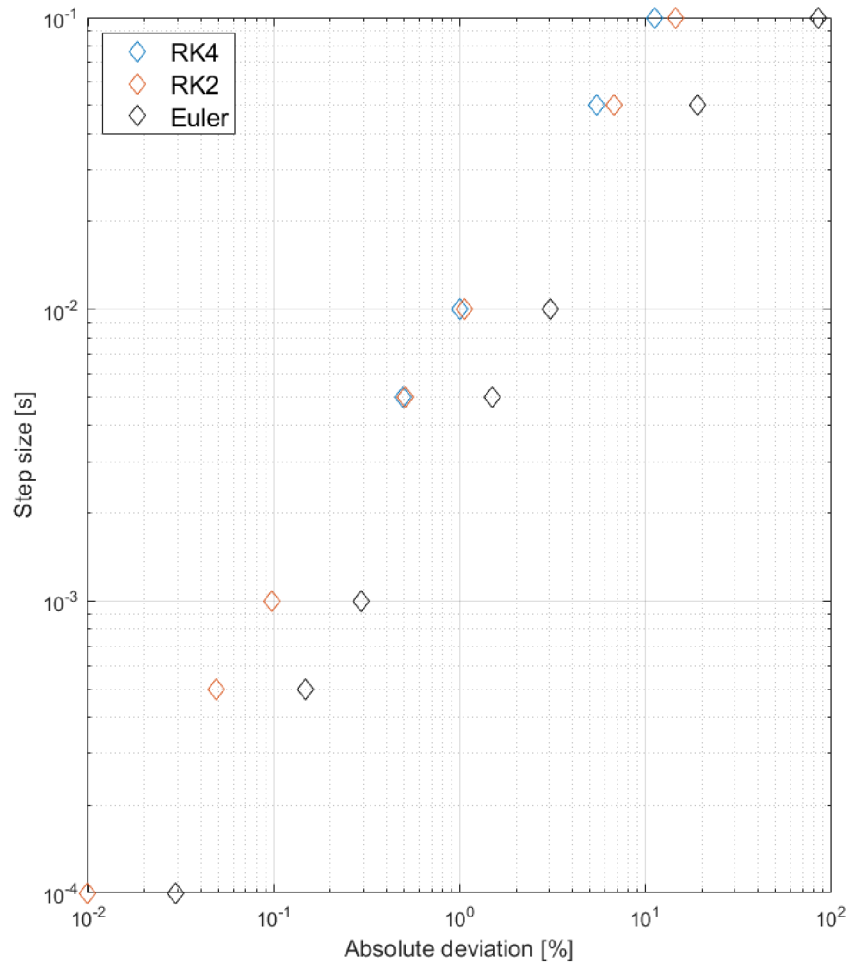
Figure 4: Logarithmic comparison between the speed and accuracy of the algorithms against the step size. Each algorithm is based on one of the defined numerical integration methods *(28), (29), (30)*.

In the following section I decided to add a complete implemented flat trajectory exterior ballistic model reduced to 2DOF (just x and y axes) using the RK2 integration method (*29*). This is the exact algorithm used in the B4E ballistic solver [9] whose results are used many times throughout this paper. Keep in mind that the solution consists of second order differential equations and therefore must be integrated twice. First integration is to find the velocity in next step assuming the acceleration throughout the time step as a constant. Second integration is to find the position of the projectile assuming the velocity throughout the time step as a constant.

Establishing the change in time:

$$t_{n+1} = t_n + h. \tag{31}$$

Solving for the velocities $v_{n+1}, v_{x_{n+1}}, v_{y_{n+1}}$:

$$k_1 = \frac{C_x \cdot \rho \cdot S \cdot v_n^2}{2 \cdot m \cdot h},$$

$$k_2 = \frac{C_x \cdot \rho \cdot S \cdot (v_n - k_1)^2}{2 \cdot m \cdot h}, \tag{32}$$

$$v_{n+1} = v_n + \frac{1}{2} \cdot (k_1 + k_2),$$

$$k_1 = \frac{v_{n+1} - v_n}{v_n} \cdot v_{x_n},$$

$$k_2 = \frac{v_{n+1} - v_n}{v_n} \cdot \left(v_{x_n} - k_1\right), \tag{33}$$

$$v_{x_{n+1}} = v_{x_n} + \frac{1}{2} \cdot (k_1 + k_2),$$

$$k_1 = \frac{v_{n+1} - v_n}{v_n} \cdot v_{y_n} + g \cdot h,$$

$$k_2 = \frac{v_{n+1} - v_n}{v_n} \cdot \left(v_{y_n} - k_1\right) + g \cdot h, \tag{34}$$

$$v_{y_{n+1}} = v_{y_n} + \frac{1}{2} \cdot (k_1 + k_2).$$

Solving for the positions x_{n+1}, y_{n+1}:

$$k_1 = \left(2 \cdot v_{x_n} - v_{x_{n+1}}\right) \cdot h,$$

$$k_2 = v_{x_n} \cdot h,$$

$$x_{n+1} = x_n + \frac{1}{2} \cdot (k_1 + k_2),$$

$$(35)$$

$$k_1 = \left(2 \cdot v_{y_n} - v_{y_{n+1}}\right) \cdot h,$$

$$k_2 = v_{y_n} \cdot h,$$

$$y_{n+1} = y_n + \frac{1}{2} \cdot (k_1 + k_2).$$

$$(36)$$

Computed velocities $v_{x_{n+1}}, v_{y_{n+1}}$ (*33*), (*34*) and positions x_{n+1}, y_{n+1} (*35*), (*36*) are the inputs into the next integration step in which they are marked as v_{x_n}, v_{y_n} and x_n, y_n. Repeating this process hundreds or thousands of times yields a 2DOF flat ballistic trajectory.

3.3   Drag laws

This chapter will focus purely on the drag coefficient and its complex behavior throughout the projectile flight. Its importance is due to occurrence in the Newton´s drag equation used in numerical integrations:

$$F_D = \frac{1}{2} \cdot C_x \cdot \rho \cdot S \cdot v^2 \text{ [N]}.$$

$$(37)$$

The drag coefficient C_x, also known as C_D, is defined as a sum of many drag components. Simple exterior ballistics models acknowledge three drag components: pressure drag, wave drag, and friction drag. Each can be influenced by the projectile´s design. Depending on application, the magnitude of each component varies greatly. For example, lift induced drag is an important aspect in aviation but not so much in ballistics.

The friction drag is caused by contact of air molecules with the projectile body. Higher velocities and greater projectile surface results in increased friction drag. Regardless, the friction drag has the lowest share out of three mentioned. Meaning the longer and more "streamline" the projectile is, the less overall drag it will experience. However, the friction of air molecules with the projectile surface has a major effect on other types of drag and cannot be neglected, mainly due to its ability to create boundary layers resulting in airflow separation.

Pressure drag, also referred to as form drag, is the main drag component at subsonic velocities ($v_{Ma} < 1$ Ma) and in some cases even at supersonic velocities. The flow of air around the projectile creates two regions, high pressure at the tip/front and low pressure at the back/tail. Because of this a further division into two subcategories known as Fore-drag (Figure 5) and Base drag could be encountered. Both pressures create a force acting in the direction opposite of projectile movement.

Wave drag originates from shock waves forming on or in front of the projectile. Formation of shock waves starts when the projectile enters the transonic region (0.8 Ma $< v_{Ma} < 1.2$ Ma) and stay throughout the whole supersonic region. During and shortly after the Second World War a lot of research was done regarding the formation of shock waves and possible ways to reduce its negative effect on wave drag. As a result, multiple nose shapes offering minimum wave drag and therefore minimum overall drag at supersonic velocities had been developed, such as the ¾ power law and Sears-Haack (Figure 5) [7].
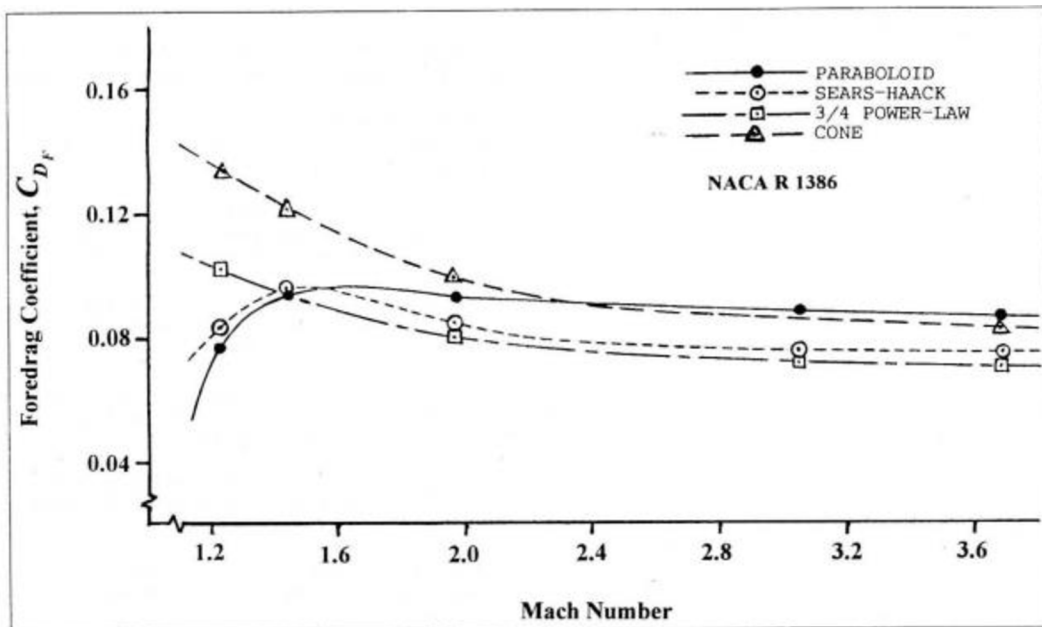

Figure 5: Foredrag coefficient (Drag coefficient at the front of the projectile and zero yaw angle) of multiple projectile nose shapes vs Mach number. Available at: [7].

Despite the deeper structured theoretical description, the drag coefficient C_x is a sum of many other drag components:

$$C_x = \sum_{i=1} C_i.$$

(38)

And the magnitude of drag components (for example wave drag) varies depending on the instantaneous velocity of the projectile:

If we determine the drag coefficient C_x at different velocities, for each velocity we get a different value. Doing so we collected a number of two-dimensional points consisting of values for drag coefficient and velocity $[v\ ;\ C_x]$, which together form the drag law. Note that due to the dependence of aerodynamical phenomena on the speed of sound, the unit of velocity is converted to Mach number $[\mathrm{Ma}\ ;\ C_x]$ or $[v_{Ma}\ ;\ C_x]$. To this day, there are countless drag laws in existence of which the most widespread are the G-Series (GL, GS, G1, ..., G8) [7]. We will mention three of them as an example, the drag law of a sphere GS, drag law G1 used for handgun or simple rifle projectiles and drag law G7 used for very low drag projectiles (Figure 6, Figure 7). The data in Figure 6 were processed from drag functions found in the book [7]. Note that in the Figure 6 a drag coefficient C_s instead of C_x is used. It is the same coefficient, only marked differently specifying that this coefficient refers only to the standard projectile (Figure 7). Drag laws are often written in tables and must be accompanied by a sketch or drawing of a standard projectile to which it refers to (Figure 7). Both must include basic projectile dimensions often given as multiples of bore diameter or radius.
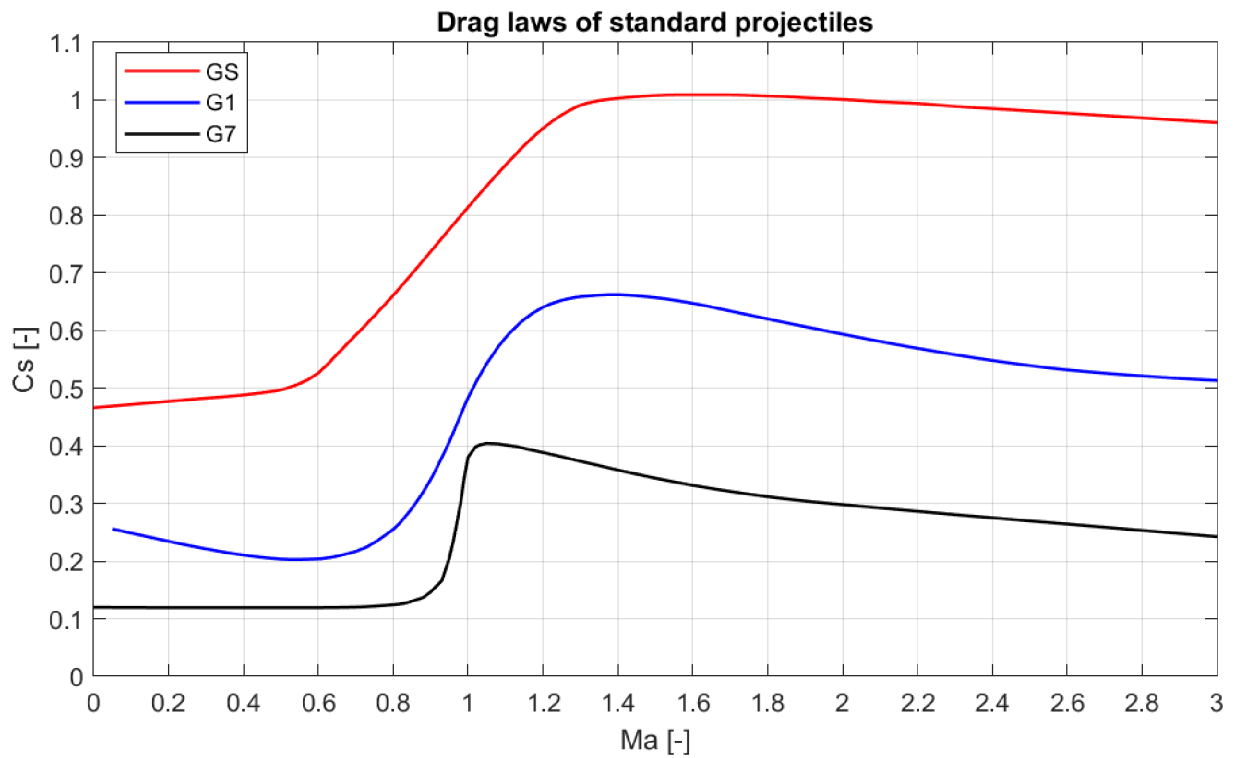
Figure 6: Drag laws (Dependence of drag coefficient on Mach number) of standard projectiles displayed in Figure 7. Both parameters are dimensionless.
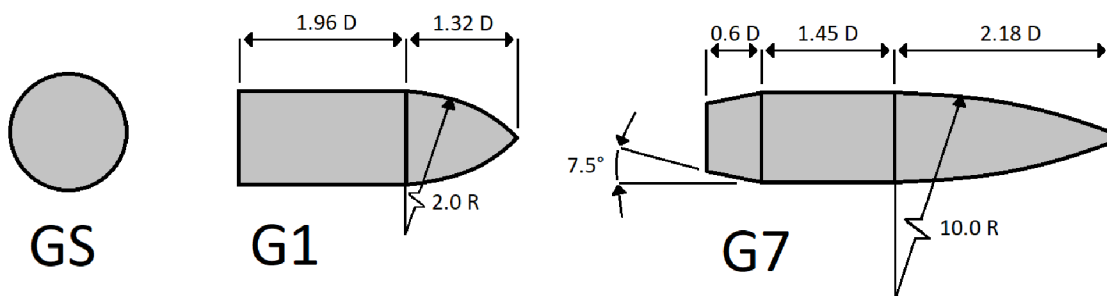

Figure 7: Sketch of standard projectiles referring to drag laws GS, G1 and G7 in Figure 6. Dimensions are referring to given diameter or radius of the bore.

The drag laws are often confused with drag functions, meaning the dependence drag force acting opposite of the projectile motion on projectile velocity. Nevertheless, computed drag function displayed in Figure 8 certainly shows the difference between the two and gives us a measure of how important projectile design is at supersonic velocities.
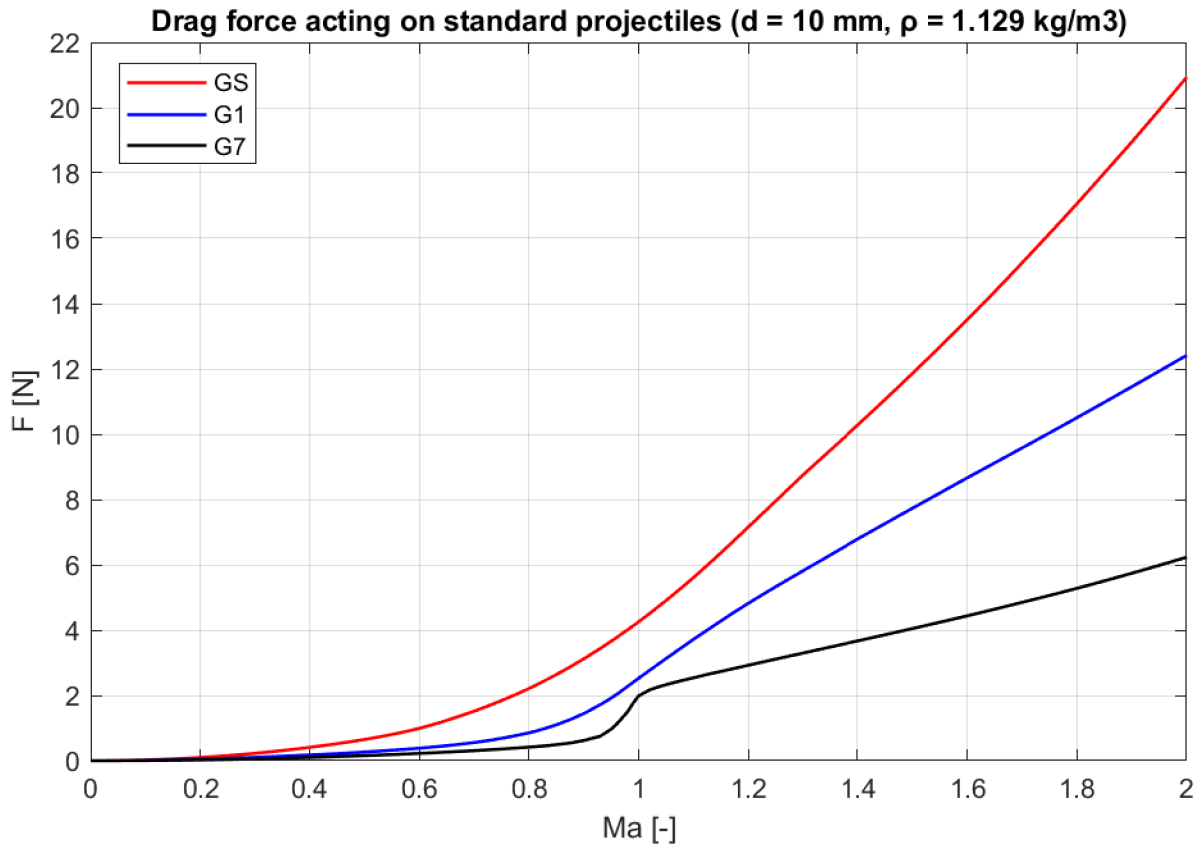
Figure 8: Drag function. Drag force acting on standard projectiles GS (red), G1 (blue) and G7 (black) ($d = 10\ mm, \rho = 1.129\ kg \cdot m^{-3}$) vs Mach number. This plot corresponds to the plot in Figure 6 when the drag coefficient (law) is implemented in the Newton´s drag equation *(37)*.

Drag laws are often neglected, mentioning only a measured value of drag coefficient C_x. The equations of motion using drag laws are in general more complicated and up to around $v_{Ma} \approx 0.5$ Ma, there is little to no benefit of not considering the drag coefficient as a constant. But as the object reaches velocities beyond that mark, it becomes a necessity.

3.4   Ballistic coefficient

Ballistic coefficient is a quantity that represents the overall ability of given projectile to overcome the air drag. Due to its simplicity, it is the most used ballistic characteristics of a projectile marketed for the common user. Simply put, the higher the ballistic coefficient, the better the projectile is at retaining its velocity. Compared to drag coefficient, the ballistic coefficient is adding projectile weight, diameter and drag law into the equation. It consists of two variables: sectional density *(41)* and the form factor *(42)*. Beware that a lot of manufacturers do not specify units. The most common units for ballistic coefficient in western markets are pounds per square inch [lb $\cdot$ in^{-2}].

$$BC = \frac{SD}{i} \qquad (40)$$

The sectional density characterizes the ratio of projectile´s cross-section to its weight:

$$SD = \frac{m}{d^2}. \qquad (41)$$

The form factor is a ratio of drag coefficient of given projectile to drag coefficient of standard projectile referring to drag law. Both coefficients must be compared at the same instantaneous velocity according to the standard projectile´s drag law. The closer the ratio of given vs standard projectile is to $i = 1$, the less error is made by using the standard projectile´s drag law as substitution for unknown drag law of given projectile. To compute the form factor, either ballistic coefficient must be known or at least one drag coefficient related to velocity must be measured.

$$i = \frac{C_x}{C_s} \qquad (42)$$

Substituting form factor *(42)* and sectional density *(41)*, we get:

$$BC = \frac{SD}{i} = \frac{m}{i \cdot d^2} = \frac{m \cdot C_s}{d^2 \cdot C_x} \ [\text{kg} \cdot \text{m}^{-2}]. \qquad (43)$$

Introducing the conversion ratio from metric to imperial units:

$$BC = \frac{m \cdot 2.20462262}{i \cdot (d \cdot 39.3700787)^2} = \frac{m \cdot C_s}{d^2 \cdot C_x} \cdot 0.00142233 \ [\text{lb} \cdot \text{in}^{-2}]. \qquad (44)$$

To demonstrate the meaning of ballistic coefficient we shall consider the following scenario: The unknown projectile drag has been measured and we obtained the following data: $d = 4.52$ mm, $m = 0.547$ g and $C_x = 0.505$ measured at velocity $v_{Ma} = 0.71$ Ma. The goal is to compare the form factors referring to the three mentioned standard projectiles GS, G1 and G7 (Figure 7) and determine the correct ballistic coefficient for the unknown projectile. From Figure 6 we obtain the drag coefficients C_s for each standard projectile at velocity $v_{Ma} = 0.7$ Ma: $\boldsymbol{C_s}(GS, v_{Ma} = 0.71 \text{ Ma}) = 0.592$, $\boldsymbol{C_s}(G1, v_{Ma} = 0.71 \text{ Ma}) = 0.217$, $\boldsymbol{C_s}(G7, v_{Ma} = 0.71 \text{ Ma}) = 0.120$.

Solving for form factors *(42)*:

$$\boldsymbol{i}(GS) = \frac{\boldsymbol{C_x}(v_{Ma} = 0.71 \text{ Ma})}{\boldsymbol{C_s}(GS, v_{Ma} = 0.71 \text{ Ma})} = \frac{0.505}{0.592} = 0.85,$$

$$\boldsymbol{i}(G1) = \frac{\boldsymbol{C_x}(v_{Ma} = 0.71 \text{ Ma})}{\boldsymbol{C_s}(G1, v_{Ma} = 0.71 \text{ Ma})} = \frac{0.505}{0.217} = 2.33,$$

$$i(G7) = \frac{C_x(v_{Ma} = 0.71 \text{ Ma})}{C_s(G7, v_{Ma} = 0.71 \text{ Ma})} = \frac{0.505}{0.120} = 4.21.$$
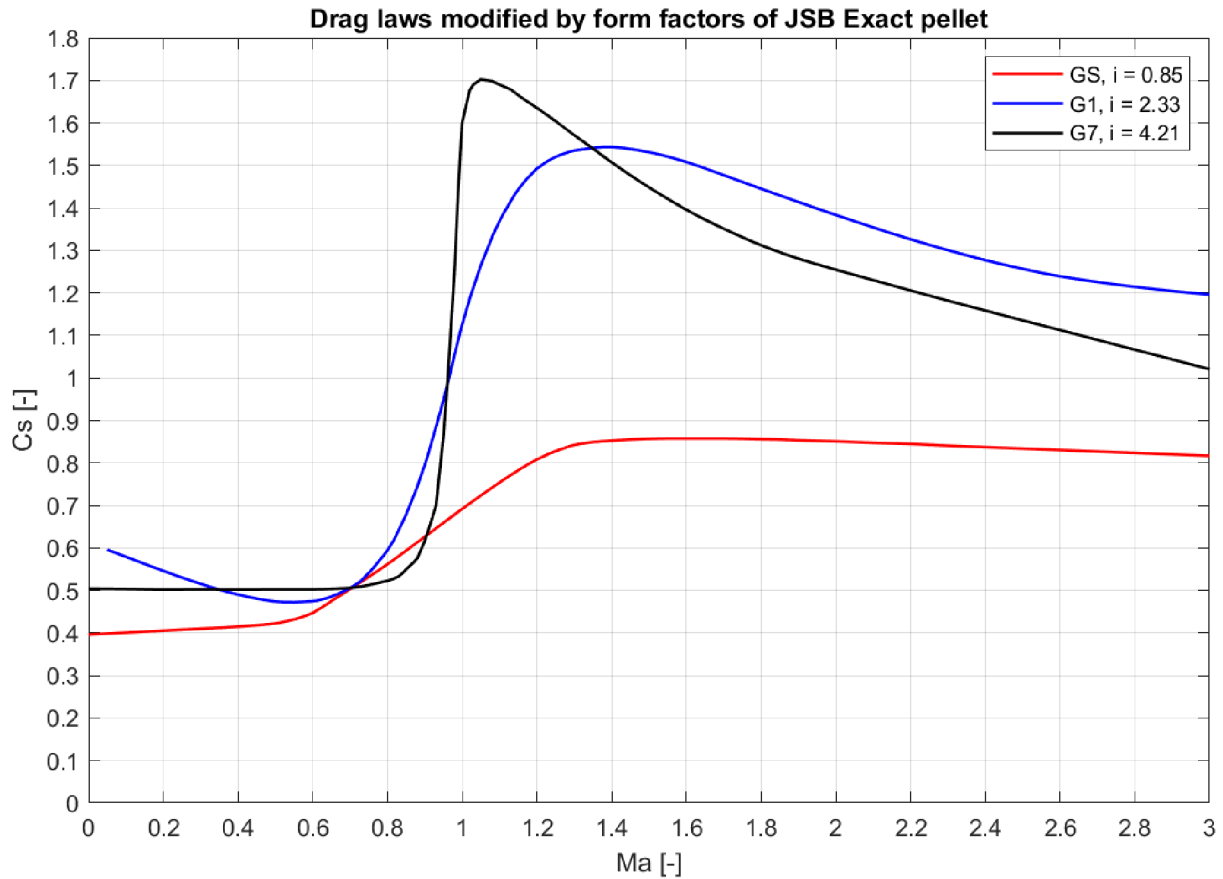

Figure 9: Possible drag laws of JSB Exact projectile created by modifying the drag laws of standard projectiles GS, G1 and G7 (Figure 6) by form factors (*42*).

The closest reference projectile from the test set compared to our pellet would be the sphere, referring to drag law GS. The plotted modified drag laws can be seen in Figure 9. Note that the form factor i is not always a constant and may vary depending on the velocity at which the drag coefficient C_x has been measured. To achieve more accurate results, we would have to evaluate it at multiple different velocities. Unfortunately, most ballistic solvers doesn´t support the drag law GS. So again, choosing the closest option possible, which happens to be the drag law G1 (*44*):

$$BC(G1) = \frac{m \cdot C_s(G1)}{d^2 \cdot C_x} \cdot 0.00142233 = \frac{0.000547 \cdot 0.217}{0.00452^2 \cdot 0.505} \cdot 0.00142233 = 0.016 \text{ lb} \cdot \text{in}^{-2}.$$

This is a valid and least expensive option of determining the ballistic coefficient based on the estimated similarity of different projectile´s drag law. Doing so, we completed the task but also introduced an error resulting from the difference of compared projectile quantified by the form factor.

Additionally, ballistic coefficient can also be substituted into differential equation of projectile acceleration. By canceling projectile weight and diameter it creates simplified and less demanding form of equation. The projectile weight is still required for muzzle and impact energy calculations, so it is not much of an advantage overall. Expressing acceleration of the projectile from Newton´s drag equation and second law of motion *(37)*, *(49)*:

$$a = \frac{C_x \cdot S \cdot \rho \cdot v^2}{2 \cdot m} = \frac{\dfrac{C_x \cdot \pi \cdot d^2 \cdot \rho \cdot v^2}{4}}{2 \cdot m} = \frac{C_x \cdot \pi \cdot d^2 \cdot \rho \cdot v^2}{8 \cdot m}.$$

(45)

Expressing the drag coefficient from final ballistic coefficient equation *(44)*:

$$C_x = \frac{m \cdot C_s}{d^2 \cdot BC} \cdot 0.00142233.$$

(46)

Substituting drag coefficient into the acceleration equation *(45)* we get projectile acceleration as a function of velocity:

$$a = \frac{\dfrac{m \cdot C_s \cdot \pi \cdot d^2 \cdot \rho \cdot v^2}{d^2 \cdot BC}}{8 \cdot m} \cdot 0.00142233 =$$

$$= \frac{C_s \cdot \pi \cdot \rho \cdot v^2}{8 \cdot BC} \cdot 0.00142233 \ [\mathrm{m} \cdot \mathrm{s}^{-2}].$$

(47)

4 MODELING THE JSB EXACT PROJECTILE IN THE PRODAS V3 SOFTWARE

PRODAS V3 is a software made by Arrow Tech Associates, Inc. used mainly for designing and modelling of missiles and projectiles. It offers detailed analysis of aerodynamical properties, interior ballistics, and terminal ballistics. The name PRODAS is an acronym for Projectile Rocket Ordnance Design and Analysis System. Since PRODAS was made for analysis of military grade weapons (artillery shells, armor piercing rounds, precision guided munitions, …) and their effects on potential targets, the user is required to have a U.S. State Department approved export license before obtaining the software. I was given the opportunity to work with PRODAS through Department of Weapons and Ammunition at University of Defense in Brno.

PRODAS can offer a lot of data, but for the purposes of this work we only need to focus on a drag law estimation of the JSB Exact projectile (JSBE).
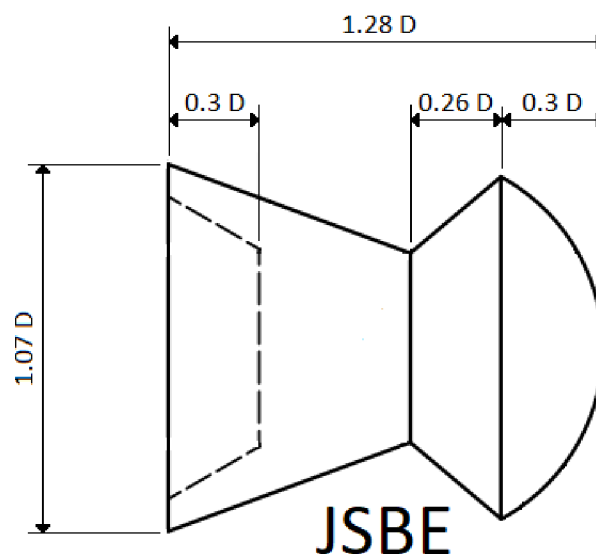

Figure 10: Authorized sketch of a JSB Exact projectile (Diabolo type projectile). Variable D [mm] expresses the diameter of the bore.

Upon request, the company JSB Match Diabolo provided a complete drawing of JSB Exact projectile (pellet). The drawing is considered as a manufacturing secret; therefore, only sketch (Figure 10) of the projectile with dimensions authorized by the manufacturer can be published. Based on the drawing a model of the projectile was created and analyzed and the result is an estimation of the JSB Exact projectile drag law (Figure 11, Table 6).
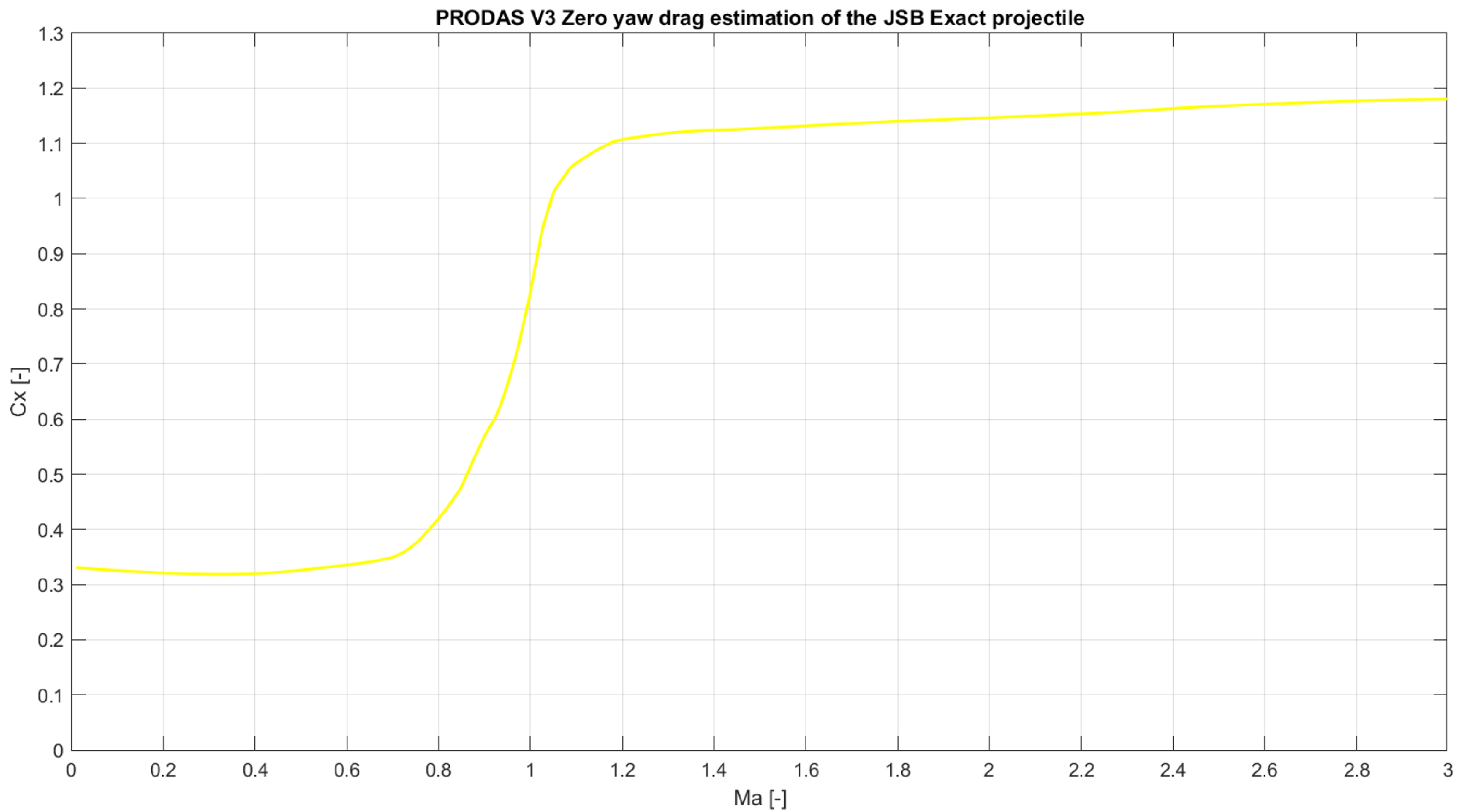
Figure 11: PRODAS V3 drag law estimation curve of the JSB Exact projectile (Figure 10).

Mach number Ma $[-]$	Drag coefficient C_x $[-]$	Mach number Ma $[-]$	Drag coefficient C_x $[-]$
0.000	0.3309	1.050	1.0108
0.400	0.3199	1.100	1.0646
0.600	0.3357	1.200	1.1071
0.700	0.3491	1.350	1.1221
0.750	0.3747	1.500	1.1275
0.800	0.4198	1.750	1.1381
0.850	0.4771	2.000	1.1465
0.875	0.5244	2.250	1.1556
0.900	0.5692	2.500	1.1677
0.925	0.6047	3.000	1.1807
0.950	0.6615	3.500	1.1834
0.975	0.7357	4.000	1.1722
1.000	0.8295	4.500	1.1654
1.025	0.9401	5.000	1.1592

Table 6: PRODAS V3 drag law estimation of the JSB Exact projectile (Figure 10).

5 MEASUREMENT AND ITS PROCESSING

As of now, we have all the theoretical knowledge to determine the drag law of the JSB Exact projectile (pellet) when given the right data. In this chapter we will focus on the possible ways to select, obtain, process and evaluate these data. Additional attention will be given to selection, capabilities and examination of the tools and devices used for measurements.

5.1 Definition of fundamental variables

F_D [N] – Drag force

ρ [kg $\cdot$ m^{-3}] – Air density

ρ_{da} [kg $\cdot$ m^{-3}] – Dry air density

p [Pa] – Air pressure

p_{da} [Pa] – Partial pressure of dry air

$r_{da} = 287.050$ [J $\cdot$ kg$^{-1} \cdot$ K^{-1}] – Specific gas constant of dry air

T [K] – Absolute air temperature

T_C [°C] – Relative air temperature

c [m $\cdot$ s^{-1}] – Speed of sound

c_{da} [m $\cdot$ s^{-1}] – Speed of sound in dry air

a [m $\cdot$ s^{-2}] – Acceleration of the projectile

v [m $\cdot$ s^{-1}] – Velocity of the projectile

x [m] – Position of projectile from origin in $x-$axis

L [m] – Distance between chronographs (Chronograph spacing)

l [m] – Distance between chronograph optical sensors

t [s] – Time of projectile movement

$t_{Student}$ [−] – Critical value of Student´s distribution

S [m^2] – Cross-sectional area of the projectile

d [m] – Diameter of the projectile

m [kg] – Weight of the projectile

C_x [−] – Drag coefficient

E [J] – Energy

W [J] – Work

n [−] – Number of measurements

k [−] – Number of degrees of freedom

$\overline{W}_\alpha$ [−] – Critical file of Student´s distribution

$\overline{x}$ [m · s^{-1}, ft · s^{-1}] – Arithmetic mean of projectile´s velocity

$\widetilde{x}$ [m · s^{-1}, ft · s^{-1}] – Median of projectile´s velocity

s^2 [m^2 · s^{-2}, ft^2 · s^{-2}] – Variance of projectile´s velocity

s [m · s^{-1}, ft · s^{-1}] – Standard deviation of projectile´s velocity

5.2 Methods of measurement

First, the measured variables must be selected. Let´s start with the atmospheric conditions during the measurement session. For computation of the dry air density and the speed of sound we can use equations *(4)*, *(10)*, *(23)* derived in the first chapter, thus only requiring data of air temperature and altitude. Temperature will be measured with standard digital thermometer commonly used in houses, as the computation do not require high measurement precision. Altitude can be read from the contour lines on the map often done by online map browsers such as https://developer.mapy.cz/rest-api/tutorialy/zjisteni-nadmorske-vysky-pomoci-rest-api/.

As we already know, drag law consists of a set of points and each of those points consists of velocity and drag coefficient [v_{Ma} ; C_x]. Unfortunately, neither can be directly measured, but both can be expressed as change in projectile position over time. Velocity can be described directly as a change of projectile position over time:

$$v = \frac{\mathrm{d}x}{\mathrm{d}t}.$$

(48)

To describe drag coefficient as a change of position over time, we need to add Newton´s drag equation *(37)* into the Newton´s second law of motion *(49)*:

$$F = m \cdot a, \qquad\qquad (49)$$

$$F = F_D => m \cdot a = \frac{1}{2} \cdot C_x \cdot \rho \cdot S \cdot v^2. \qquad (50)$$

Expressing the drag coefficient from the resulting equation *(50)* and substituting differential forms of acceleration and velocity we get:

$$C_x = \frac{2 \cdot m \cdot a}{\rho \cdot S \cdot v^2} = \frac{2 \cdot m}{\rho \cdot S} \cdot \frac{a}{v^2} = \frac{2 \cdot m}{\rho \cdot S} \cdot \frac{\frac{dv}{dt}}{\left(\frac{dx}{dt}\right)^2} = \frac{2 \cdot m}{\rho \cdot S} \cdot \frac{d^2x}{dt^2} \cdot \left(\frac{dx}{dt}\right)^{-2}. \qquad (51)$$

The reason behind equation *(51)* is to prove that both drag coefficient and projectile velocity can be expressed by the projectile´s position as a function of time. This allows the use of numerous different measurement outputs if they involve at least one combination of acceleration a, velocity v, position x or time t.

In general, there are two common types of devices used for measurement in external ballistic of small arms projectiles: Doppler radars (Figure 12) and Optical chronographs (Figure 13).
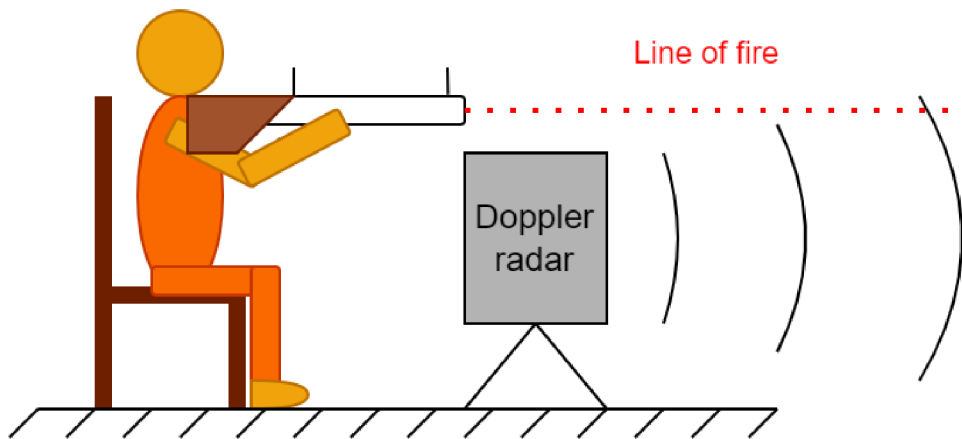

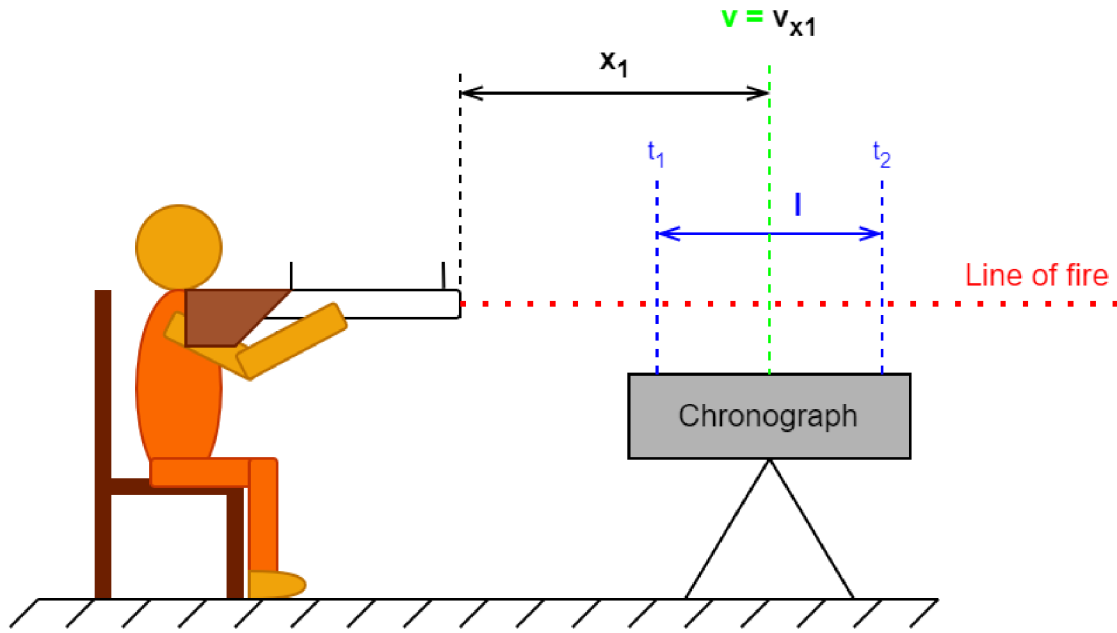Figure 12: Illustration of the Doppler radar measurement platform.

Figure 13: Illustration of the Optical chronograph measurement platform.

The Doppler radar measures the change of projectile´s position over time. Optical chronograph measures the time it takes the projectile to travel a given distance. The Doppler radars are superior in terms of accuracy and in amount of available data. Unfortunately, they are very expensive. The affordability of optical chronographs is much better, therefore I decided to use them. Unlike Doppler radar, optical chronograph displays just the average projectile velocity. However, using two optical chronographs placed in series (Figure 14) while knowing the distance between them, we will get the change in projectile velocity over distance $[\Delta v; L]$. Measured velocities are marked gradually – Chronograph C_1 measures velocity v_1 and Chronograph C_2 measures velocity v_2 (Figure 14).
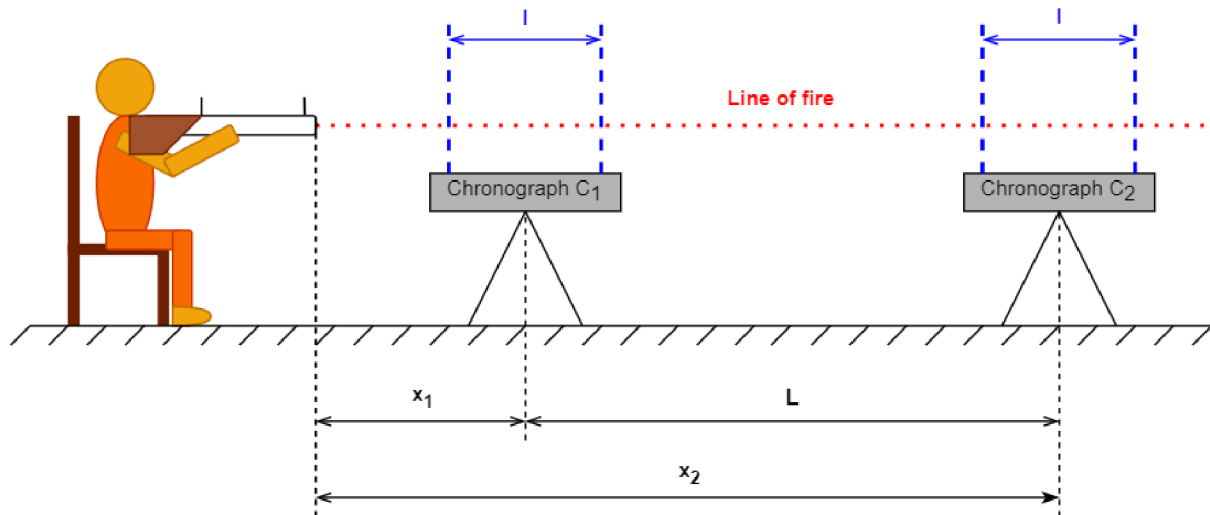
Figure 14: Illustration of two optical chronographs placed in series. This exact platform was used to measure the change in projectile velocity at a given distance.

For the project I chose a set of two Caldwell Ballistic Precision Chronographs one of which I bought with additional LED lighting source to reduce the number of failed measurements caused by poor lighting conditions. The Caldwell Ballistic Precision Chronograph displays velocity readings as an integer either in meters per second $[\text{m} \cdot \text{s}^{-1}]$ or feet per second $[\text{ft} \cdot \text{s}^{-1}]$. Measuring in feet per second offers a finer scale, therefore the measurements will be recorded in feet per second and later converted to meters per second $1 \, \text{ft} \cdot \text{s}^{-1} = 0.3048 \, \text{m} \cdot \text{s}^{-1}$.

To cover the entire subsonic region multiple airguns have been used, one of which had the option to regulate air pressure in the piston allowing the pellet to achieve a wide range of muzzle velocities. The airguns used were Benjamin 397S (regulated piston pressure), Gamo Hunter 440 and Crosman Quest NP. All of them were thoroughly tested and provided low initial velocity extreme spread and consistent accuracy up to a 30 m distance.

5.3 Platform optimization

Before each set of measurements, the platform must be optimized to achieve a balance between the magnitude of projectile velocity decrease and the chronograph spacing. To proceed we must make few simplifications about the nature of the measurements: during the motion of projectile in the section L (between the chronographs) the force of gravity acting on the projectile is neglected and an assumption that the drag force has a constant value is made (Figure 15). Meaning the deceleration of the projectile is constant, the decrease in velocity is linear and the total traveled distance is equal to the chronograph spacing L.
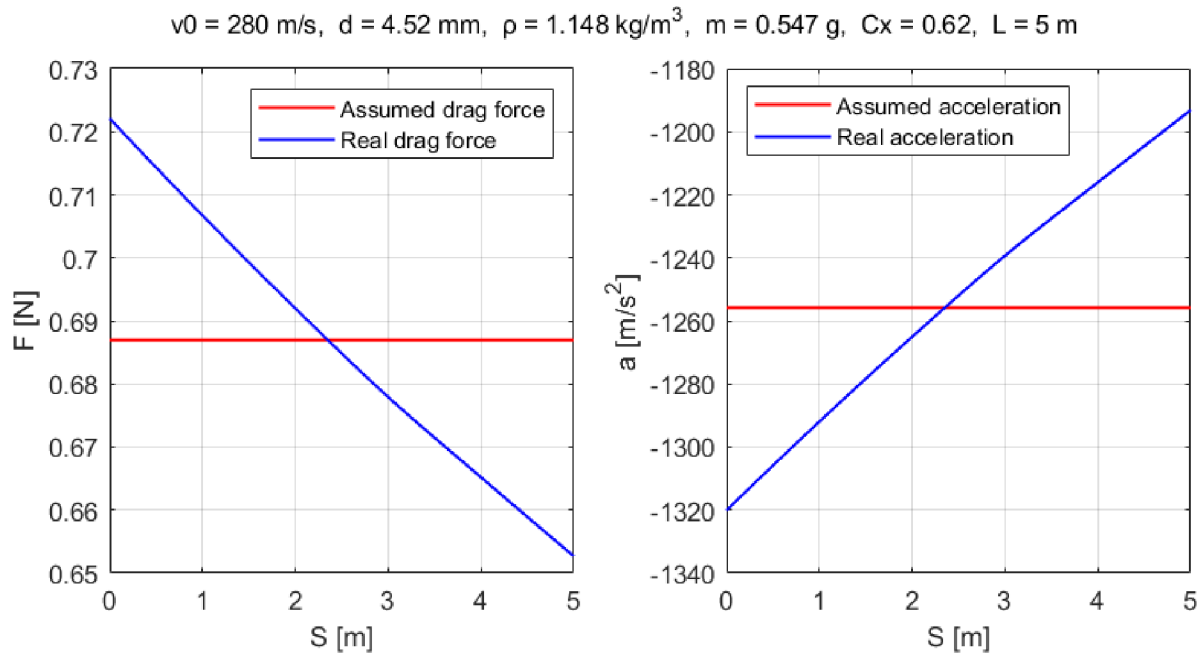
36

Figure 15: The differences between assumed and real value of drag force and acceleration of the JSB Exact projectile. Data in figures have been computed using the Newton´s drag equation (37) and the B4E solver [9].

The magnitude the chronograph spacing L depends on the projectile initial velocity and drag. Theoretically, smaller spacing results in decrease of the linear assumption error (Figure 16), but simultaneously increases the platform measurement error. Considering all factors, I decided the ideal Chronograph spacing for the JSB Exact projectile should be around $L = 5$ m (Figure 16), whereas I changed the spacing between $L = 2$ m at the higher and $L = 8$ m at the lower velocity measurement sets.

The reason behind this paragraph can be fully understood after examining Chapter 4: Measurement and its processing. Theoretically you would want to place the chronographs as close to each other as possible to replicate the function of Doppler radar, practically it has no use. The setup just isn't accurate enough to measure such incremental differences in projectile velocity and the measurement error bar could easily exceed the measured differences in velocity. Placing the chronographs too far from each other has no use either, because of the nature of the measured projectile. The JSB Exact projectile is small and sometimes doesn't create enough shade to trigger the optical sensors, therefore it must be shot directly above the sensors which becomes harder with increasing distance when you are simultaneously trying to get the best alignment with the chronographs while also not damaging them via inaccurate fire. For example, I tried increasing the spacing to $L = 12$ m, where the second chronograph (C_2) gave me reading on just one in five pellets. All of this is not universal and depends on a lot of factors ranging from the equipment and conditions you have. Generally, with larger projectiles like the JSB Exact King 6.35 mm you should be able to increase the spacing a lot more compared to the maximum spacing I set for the JSB Exact 4.5 mm.
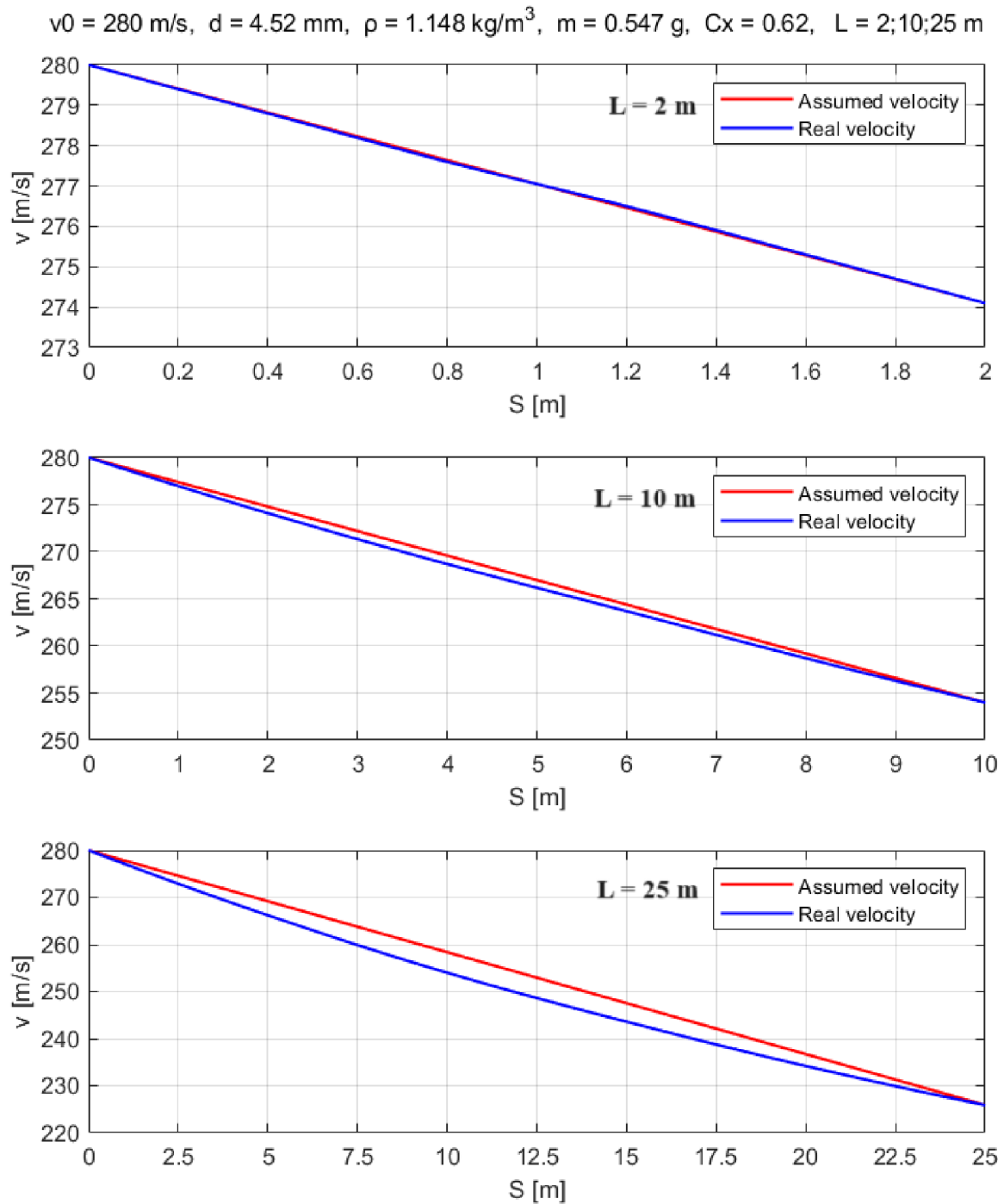
Figure 16: The differences between assumed and real value of velocity of the JSB Exact projectile depending on the chronograph spacing L ($L = 2$ m, $L = 10$ m, $L = 25$ m).

5.4 Data processing

There are many possible ways to compute the drag law points based on the measured data. As an example, I chose two of them. For both, the assumption that the projectile acceleration has a constant value applies. The first one, which I find to be easier and more intuitive, expresses

38

the drag coefficient using basic equations of motion. The second one is based on energy conservation and is thoroughly described in the book [8].

Motion approach: We start with expressing the drag coefficient from the drag equation using substitution of the drag force into the Newton´s second law of motion *(37)*, *(49)*:

$$F_{D_{mean}} = \frac{1}{2} \cdot C_x \cdot \rho \cdot S \cdot v_{mean}^2 \ [\text{N}],$$

$$F_{D_{mean}} = m \cdot a_{mean}, \tag{52}$$

$$C_x = \frac{2 \cdot m \cdot a_{mean}}{\rho \cdot S \cdot v_{mean}^2}.$$

Considering a linear distribution of velocity decrease, we can determine the average velocity of projectile in the section L:

$$v_{mean} = \frac{v_1 + v_2}{2}. \tag{53}$$

Using the average velocity *(53)*, we can compute the time it takes the projectile to travel a distance $S = L$:

$$t = \frac{L}{v_{mean}} = \frac{L}{\frac{v_1 + v_2}{2}} = \frac{2 \cdot L}{v_1 + v_2}. \tag{54}$$

Knowing the decrease in velocity over a distance $S = L$ we now have all the variables to express the absolute value of projectile mean acceleration as a function of two measured velocities and the chronograph spacing:

$$\Delta v = v_1 - v_2, \tag{55}$$

$$a_{mean} = \frac{\Delta v}{t} = \frac{v_1 - v_2}{\frac{2 \cdot L}{v_1 + v_2}} = \frac{(v_1 - v_2) \cdot (v_1 + v_2)}{2 \cdot L}. \tag{56}$$

By substituting the acceleration *(56)* and mean velocity *(53)* into the drag equation we get:

$$C_x = \frac{2 \cdot m \cdot \frac{(v_1 - v_2) \cdot (v_1 + v_2)}{2 \cdot L}}{\rho \cdot S \cdot \left(\frac{v_1 + v_2}{2}\right)^2} = \frac{4 \cdot m \cdot (v_1 - v_2)}{\rho \cdot S \cdot L \cdot (v_1 + v_2)}. \tag{57}$$

Energy approach [8]: We suggest that the work of gravity force on a small distance is equal to zero. The only force doing the work is the drag force. The work can be defined as the decrease of projectile kinetic energy:

$$W = \Delta E_k, \tag{58}$$

$$W = F_{D_{mean}} \cdot L, \tag{59}$$

$$E_k = \frac{1}{2} \cdot m \cdot v^2, \tag{60}$$

$$\Delta E_k = E_{k_1} - E_{k_2} = \frac{1}{2} \cdot m \cdot (v_1^2 - v_2^2). \tag{61}$$

The dependency of work on kinetic energy can also be written as follows:

$$\frac{1}{2} \cdot m \cdot (v_2^2 - v_1^2) = -\int_{x1}^{x2} F_D \cdot \mathrm{d}x. \tag{62}$$

Completing the integration steps, we obtain:

$$F_{D\ mean} = \frac{1}{2} \cdot m \cdot \frac{v_2^2 - v_1^2}{L} = S \cdot \frac{\rho \cdot v_{mean}^2}{2} \cdot C_x \left(\frac{v_{mean}}{a}\right), \tag{63}$$

$$C_x \left(\frac{v_{mean}}{a}\right) = \frac{4 \cdot m}{\rho \cdot S \cdot L} \cdot \frac{v_1 - v_2}{v_1 + v_2}. \tag{64}$$

Both ways achieved the same result: An equation for computation of the drag coefficient as a function of the velocity decrease on section L. Note that the drag coefficient must always relate to the mean velocity of given measurement $[v_{mean} ; C_x]$. Expressing the cross-sectional area of rotationally symmetric projectiles, we obtain the final form of the equation:

$$C_x = \frac{4 \cdot m \cdot (v_1 - v_2)}{\rho \cdot \dfrac{\pi \cdot d^2}{4} \cdot L \cdot (v_1 + v_2)} = \frac{16 \cdot m \cdot (v_1 - v_2)}{\rho \cdot \pi \cdot d^2 \cdot L \cdot (v_1 + v_2)}. \tag{65}$$

5.5 An example of drag law point computation

As a summary of the entire computation process, we will solve one point of the drag law step-by-step. To do so, we need the following data:

$$v_1 = 913 \text{ ft} \cdot \text{s}^{-1} = 278.28 \text{ m} \cdot \text{s}^{-1}, \qquad v_2 = 866 \text{ ft} \cdot \text{s}^{-1} = 263.96 \text{ m} \cdot \text{s}^{-1}$$

$$L = 4 \text{ m}, \qquad d = 4.53 \text{ mm}, \qquad m = 0.547 \text{ g}, \qquad T_C = -1.5 \,^\circ\text{C}, \qquad h = 541 \text{ m}.$$

Let´s start with determining the atmospheric condition during the measurement. Solving for air density preceded by the computation of air pressure (*10*), (*4*):

$$p \approx p_{da} = 101325 \cdot \left(1 - \frac{h}{44331}\right)^{5.2577} = 101325 \cdot \left(1 - \frac{541}{44331}\right)^{5.2577} = 94990 \text{ Pa},$$

$$\rho \approx \rho_{da} = \frac{p}{r_{da} \cdot T} = \frac{p}{r_{da} \cdot (T_C + 273.15)} = \frac{94990.4}{287.05 \cdot (-1.5 + 273.15)} = 1.218 \text{ kg} \cdot \text{m}^{-3}.$$

To display the resulting drag law as a dependency on Mach number we need to compute the speed of sound (*23*):

$$c \approx c_{da} \approx 331.3 + 0.6 \cdot T_C = 331.3 + 0.6 \cdot (-1.5) = 330.4 \text{ m} \cdot \text{s}^{-1}.$$

Solving for the Mach number ($x - $ axis coordinate) (*53*):

$$v_{mean} = \frac{v_1 + v_2}{2} = 271.12 \text{ m} \cdot \text{s}^{-1},$$

$$v_{Ma} = \frac{v_{mean}}{c} = \frac{271.12}{330.39} = 0.821.$$

Solving for the drag coefficient corresponding to v_{Ma} (*y* - axis coordinate) (*65*):

$$C_x = \frac{16 \cdot m \cdot (v_1 - v_2)}{\rho \cdot \pi \cdot d^2 \cdot L \cdot (v_1 + v_2)} = \frac{16 \cdot 0.000547 \cdot (278.28 - 263.96)}{1.218 \cdot \pi \cdot 0.00453^2 \cdot 4 \cdot (278.28 + 263.96)} = 0.7358.$$

The last step is to write the coordinates as a two-dimensional point:

$$[x; y] = [v_{Ma}; C_x] = [0.821; 0.7358].$$

5.6 Errors in measurements

A verification of the chronograph reading validity must be done prior to proceeding with the measurement itself. The manufacturer guarantees the maximum deviation for the Caldwell Precision Chronograph to be within $\pm$ 0.025 %, that is if set properly. Both chronographs must

be set on the same horizontal plane with the airgun. In my conditions this is not achievable due to the location of the safe impact zone which requires the airgun to be shoulder fired (Figure 17). Rather than verifying the manufacturer´s claims the overall deviation in a realistically achievable conditions will be verified just to rule out a potential critical error occurring during the measurement.
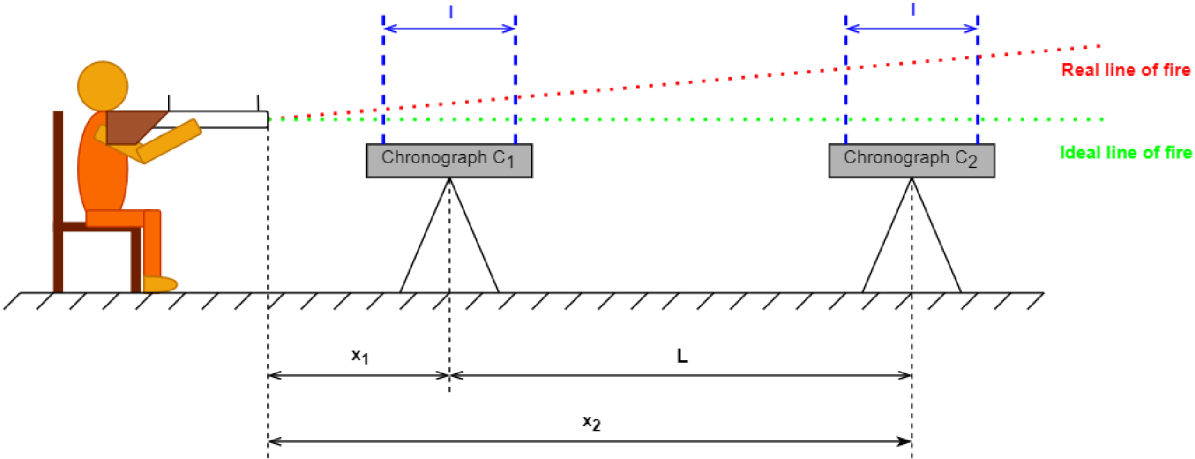

Figure 17: Illustration of the most common error in measurement. Both chronographs will measure a lower velocity than actual.

Both chronographs have been set outside in uncontrolled environment in line parallel to each other and a total of 25 JSB Exact projectiles (pellets) has been fired through each of them. Distance between airgun muzzle and each chronograph has been kept as constant as possible. To limit differences in reading due to changing muzzle velocity caused by internal gas piston heating or due to changing light conditions, the chronographs were alternated 10 times during the measurement. Statistically, the more measurements we take, the less will the computed average velocity differ and therefore the more valid the test becomes. Since the purpose of the test is to detect a potential critical error, 25 measurements for each chronograph are sufficient. Otherwise, to verify the manufacturers claims much more precise firearm, controlled environment and significant number of measurements would be needed.

Formulas for calculating basic statistical quantities - Arithmetic mean:

$$\bar{x} = \frac{1}{n} \cdot \sum_{i=1}^{n} f_i \cdot x_i.$$

(66)

Median:

$$\tilde{x} = \frac{1}{2} \cdot \left(x_{\frac{n}{2}} + x_{\frac{n}{2}+1} \right).$$

(67)

Variance:

42

$$s^2 = \left(\frac{1}{n} \cdot \sum_{i=1}^{n} f_i \cdot x_i^* \right) - \bar{x}^2. \tag{68}$$

Standard deviation:

$$s = \sqrt{s^2}. \tag{69}$$

	Chronograph C_1	Chronograph C_2	$C_1 - C_2$
$\bar{x}$ [ft·s^{-1}]	772.84	768.92	3.92
$\hat{x}$ [ft·s^{-1}]	773	778	6
$\tilde{x}$ [ft·s^{-1}]	772	768	4
s^2 [ft^2·s^{-2}]	8.8544	20.0736	19.5936
s [ft·s^{-1}]	2.9756	4.4803	4.4264

Table 7: Computed basic statistical quantities.

As expected, the difference between the readings (Table 7) is order of magnitude higher than the guaranteed percentage given by manufacturer. Despite this, the setup is still getting a more than enough accuracy-well within ±1 % error. Judging based on the available data, the C_1 chronograph (without artificial light source) measured on average 0.51 % higher velocities than the C_2 chronograph. To confirm this claim, we can test it on 95 % confidence level if we consider the measured velocities to be in a Student´s distribution.

Coefficient of Student's distribution for 95 % confidence interval:

$$k = n - 1 = 24, \tag{70}$$

$$t_{Student\ 1-\frac{\alpha}{2}}(k) = t_{Student\ 0.975}(24) = 2.064. \tag{71}$$

Testing hypothesis $H_0: \mu(C_1 - C_2) = 0$ compared to alternative hypothesis $H_A: \mu(C_1 - C_2) \neq 0$, $\alpha = 0.05$:

$$t_{Student} = \frac{\bar{x}(C_1 - C_2)}{s(C_1 - C_2)} \cdot \sqrt{k} = \frac{3.92}{4.4264} \cdot \sqrt{24} = 4.3385, \tag{72}$$

$$\overline{W}_\alpha = \langle -t_{Student\ 1-\frac{\alpha}{2}}(k), \quad t_{Student\ 1-\frac{\alpha}{2}}(k) \rangle = \langle -2.064, \quad 2.064 \rangle, \tag{73}$$

$$t_{Student} \notin \overline{W}_\alpha.$$

Therefore, we can say with 95 % certainty (*73*) that the chronograph C_1 would give us higher velocity reading than the chronograph C_2.

6 DRAG LAW JSBE

Overall, over 500 measurements were taken and processed, 474 of which were non faulty. We will call them individual measurements and they will serve as a basis for further statistical data processing. Individual measurements (Figure 18) were taken in groups. Each group has its own data about air temperature, projectile diameter, projectile initial velocity and chronograph spacing. Each group is also represented by the arithmetic mean of drag coefficient and arithmetic mean of Mach number (Figure 19). The standard deviation error bars have not been included to preserve the clarity of the graph.

Groups with very similar average velocities were again combined, using the arithmetic mean to form the averages of groups or clusters (Figure 20). Based on the averages of groups an extrapolation curve (Figure 21) was generated in software MATLAB R2022b using the Modified Akima (makima) interpolation function. The extrapolation curve serves just as a personal estimate of the drag law therefore its base points were artificially created to represent the smooth increase/decrease of drag coefficient.

The last step is approximation of the drag coefficient value where it has not been measured (Figure 22, Table 8). This is not directly necessary in terms of publishing the results, but it must be done due to its use in ballistic software where the user can enter a higher velocity $v_{Ma} \gg$ 1 Ma. The base points for approximation were also created artificially based on the measured data and PRODAS V3 drag law and interpolated with the Modified Akima (makima) function.
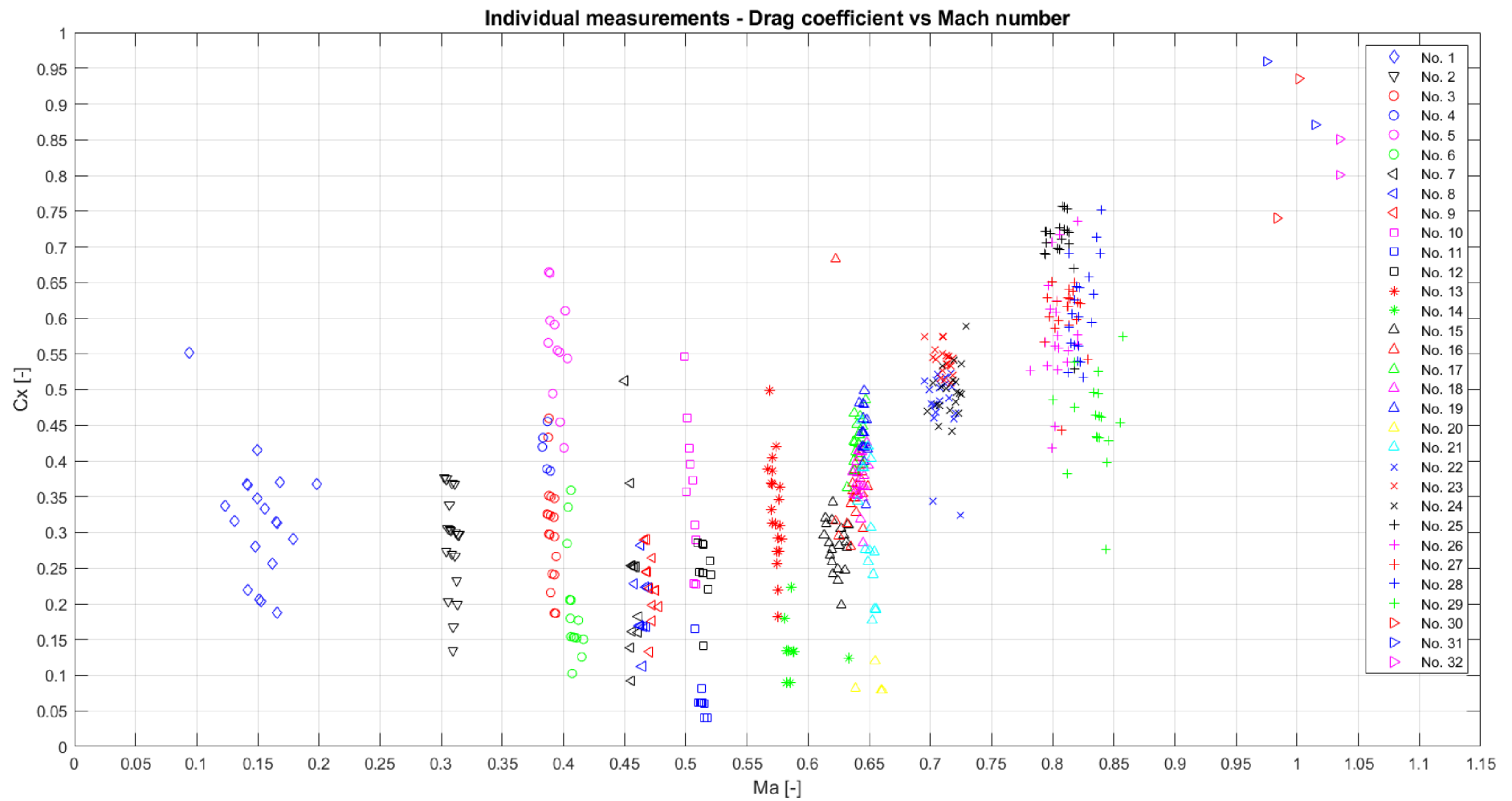
Figure 18: Evaluated non-faulty individual measurements divided into 32 groups.

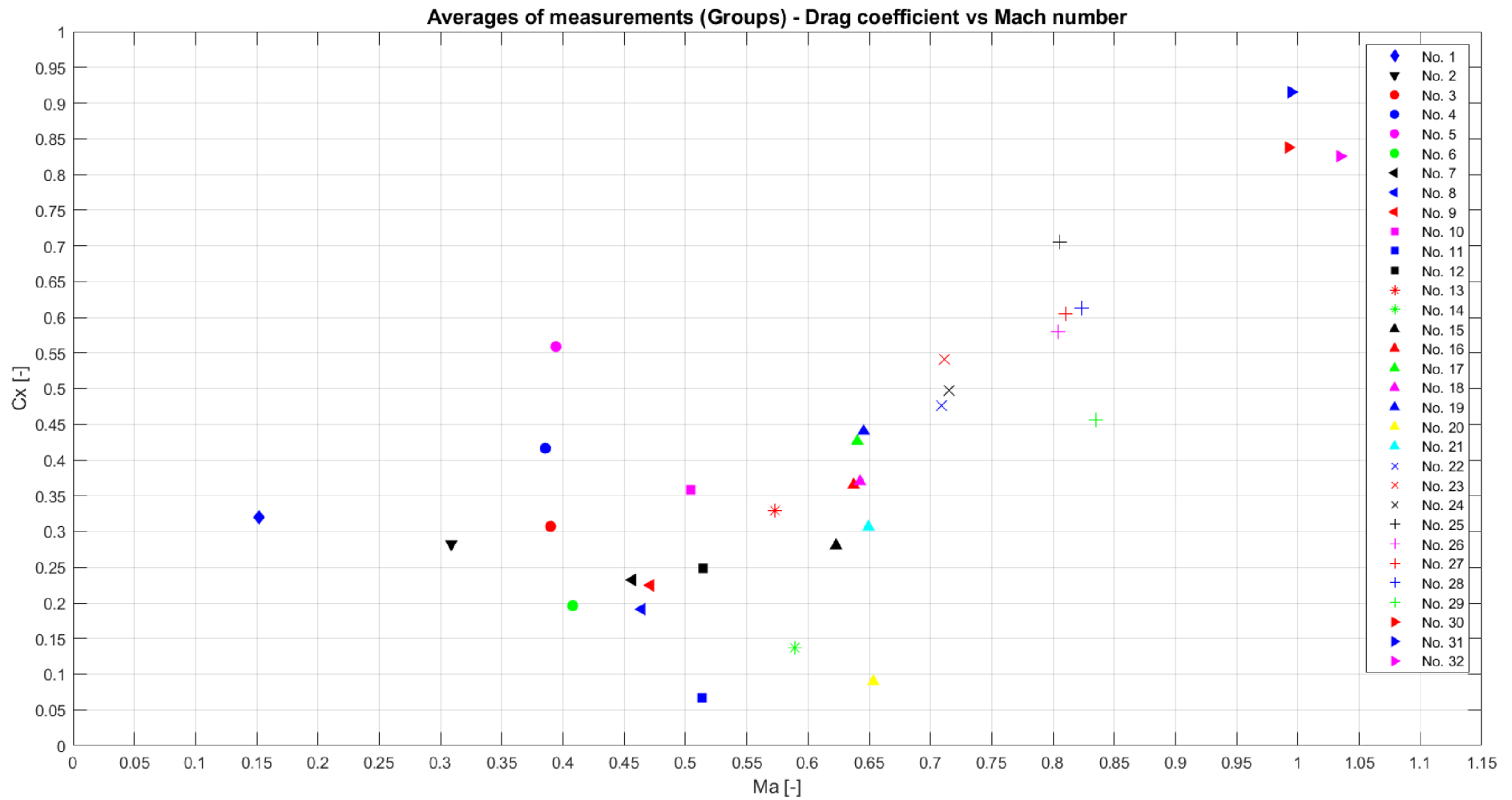Figure 19: The arithmetic averages of Mach number and drag coefficient taken from each measurement group. Values are displayed without the standard deviation error bars to maintain clarity.
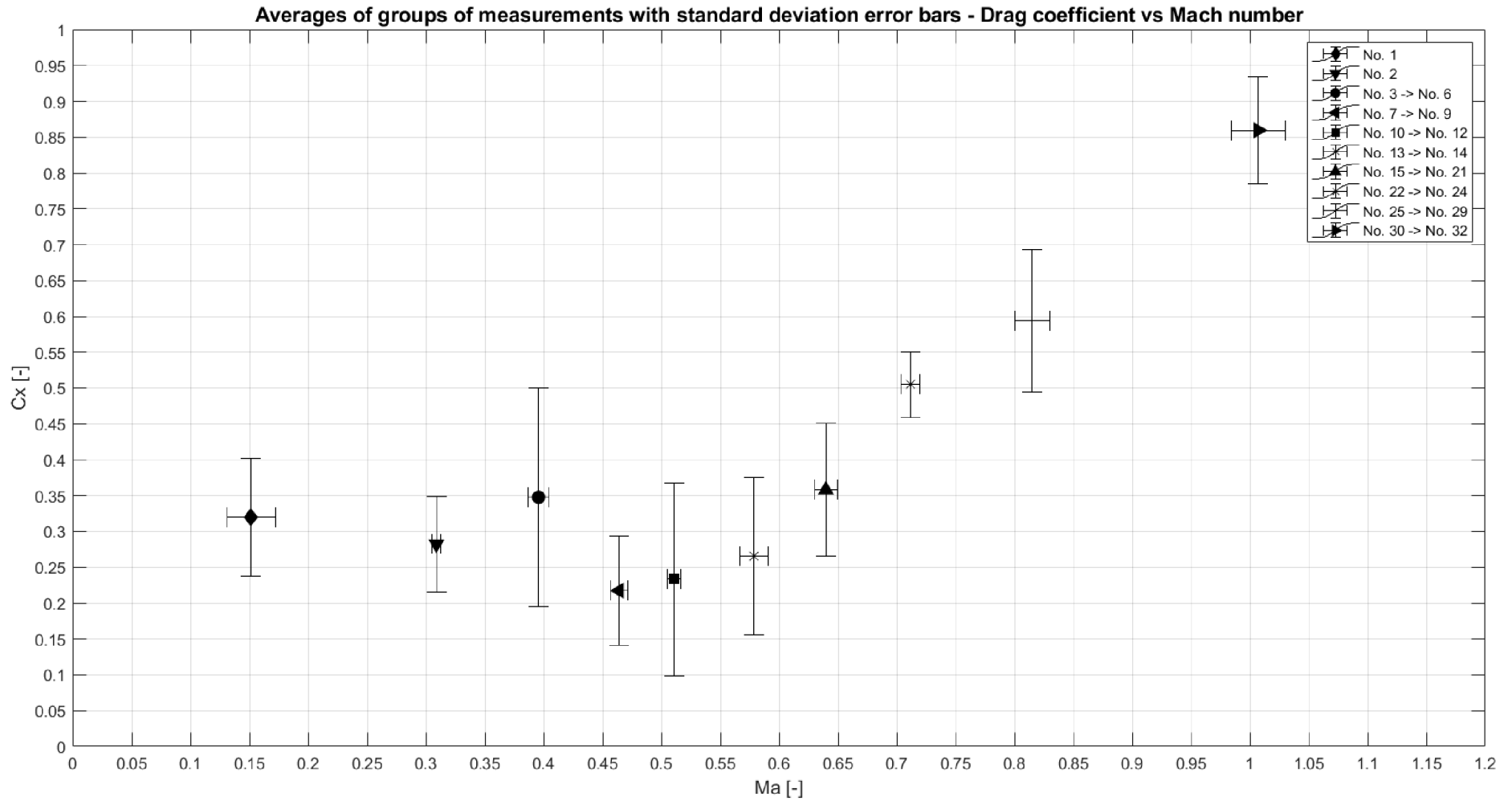
Figure 20: The arithmetic averages of clusters of groups linked based on similar average value of velocities. Each point has error bars consisting of standard deviation of the drag coefficient (y-axis) and Mach number (x-axis).
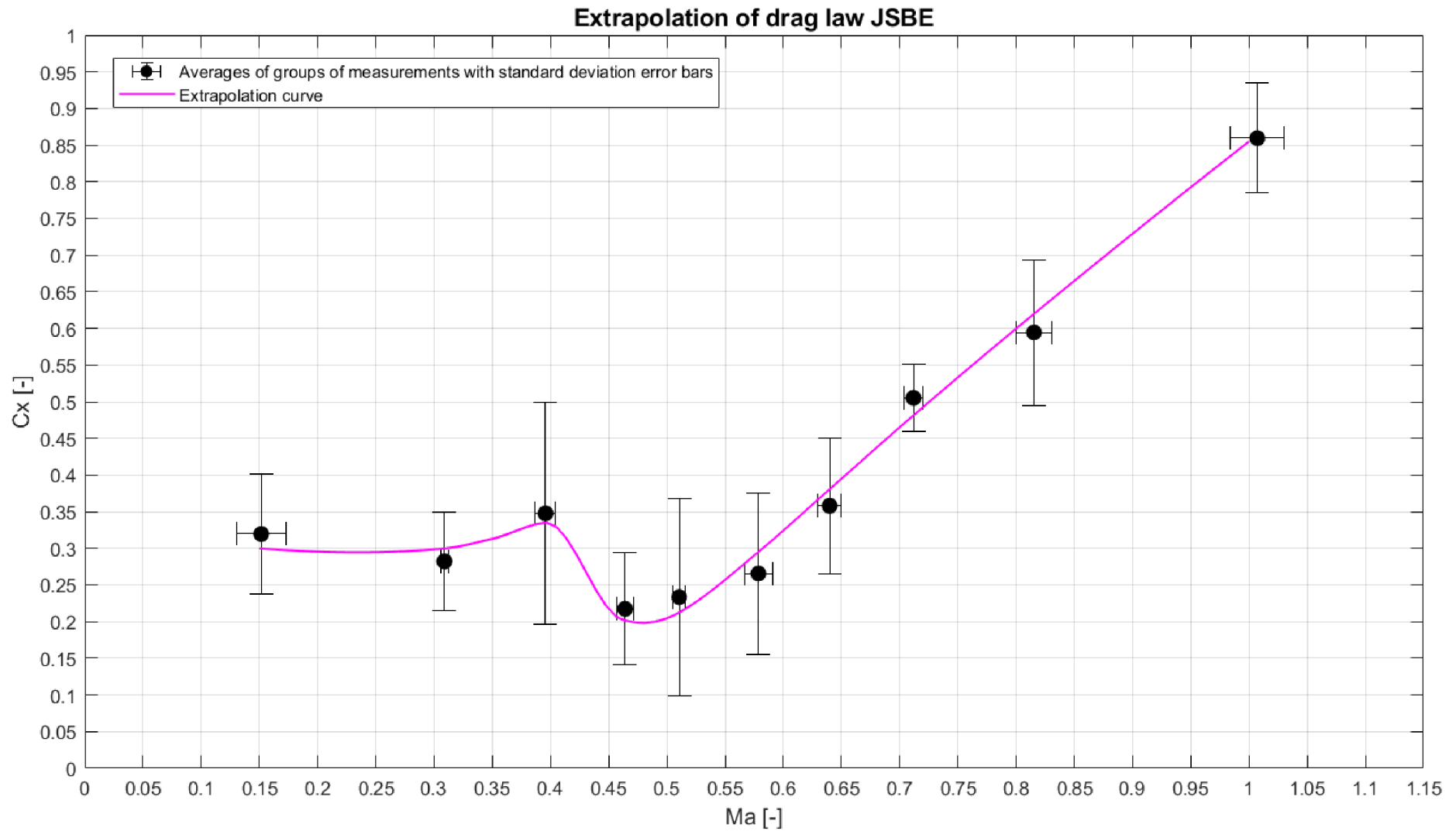
Figure 21: Interpolation curve of drag law JSBE generated by MATLAB Modified Akima function. The curve is based on artificially extrapolated points created from the averages of groups of measurements (averages of clusters of groups) to represent the smooth gradual increase in drag coefficient.

Figure 22: Approximation of the drag law JSBE (red) based on the PRODAS V3 drag law approximation, measured and extrapolated data. This figure represents the final form of drag law JSBE.

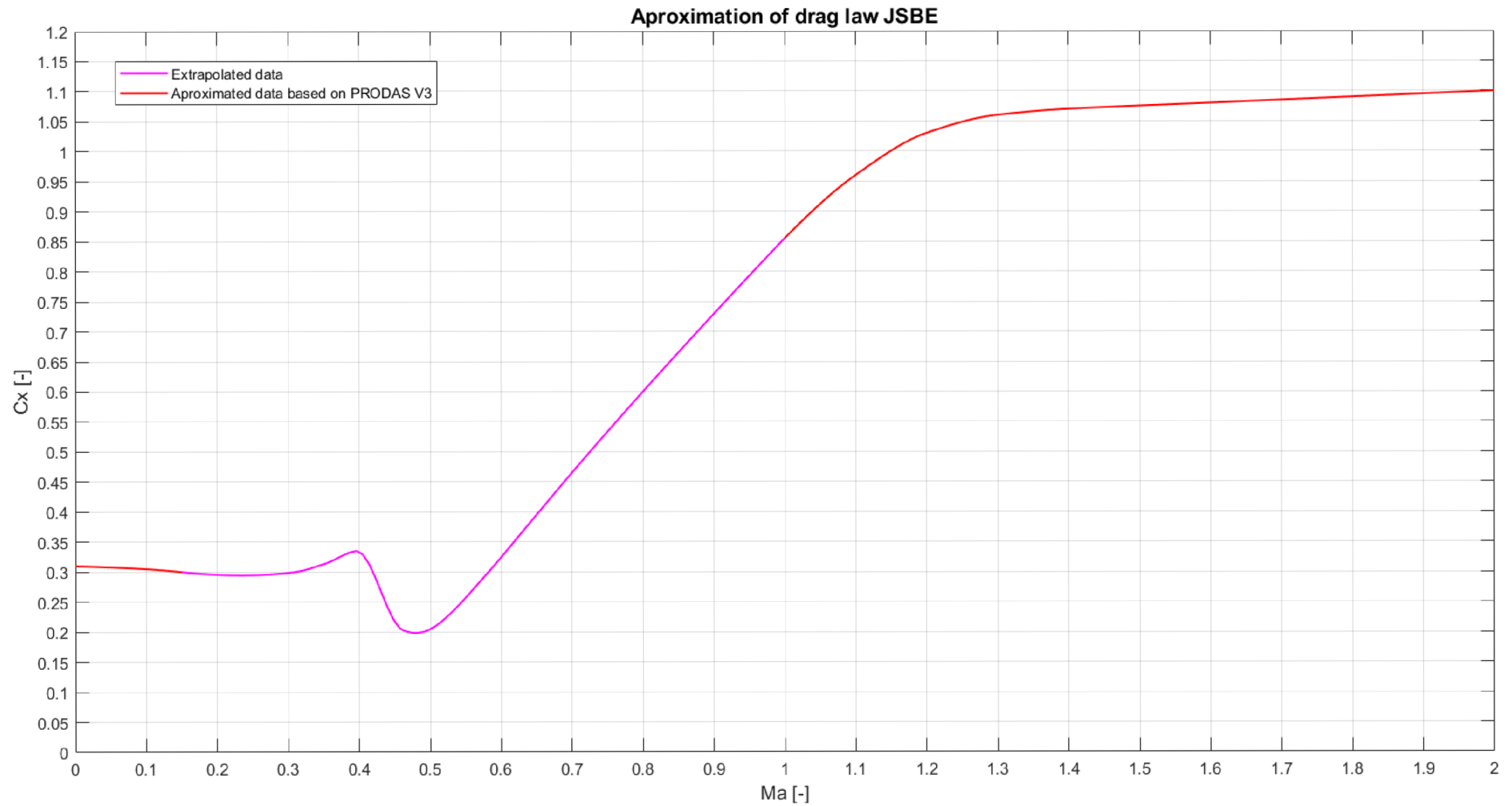| Mach number Ma $[-]$	Drag coefficient C_s $[-]$	Mach number Ma $[-]$	Drag coefficient C_s $[-]$
0.00	0.310	0.70	0.465
0.05	0.308	0.75	0.531
0.10	0.305	0.80	0.600
0.15	0.300	0.85	0.665
0.20	0.295	0.90	0.728
0.25	0.295	0.95	0.794
0.30	0.299	1.00	0.855
0.35	0.313	1.10	0.960
0.40	0.332	1.20	1.030
0.45	0.212	1.30	1.060
0.50	0.208	1.40	1.070
0.55	0.256	1.60	1.080
0.60	0.324	1.80	1.090
0.65	0.395	2.00	1.100

Table 8: Drag law JSBE consisting of extrapolated points (white) and approximated points (red).

Between $v_{Ma} \approx 0.40$ Ma and $v_{Ma} \approx 0.60$ Ma I measured a strange sudden decrease in drag coefficient. To exclude the possibility of measurement error I recreated the group measurement twice and confirmed the steep decrease. In my opinion this effect is related to sudden change in airflow around the projectile (boundary separation layer). Investigating this phenomenon requires a detailed step by step measurement with at least two airguns of different calibers (boundary layer separation depends on the projectile diameter) with the possibility to increase the muzzle velocity by fraction of magnitude compared to the airgun Benjamin 397S. Purchasing additional firearms would be indeed too expensive for this project. Therefore, I leave this subject open for additional research.

7 RESULTS COMPARISON

There are numerous ways to verify the accuracy of a drag law, or to compare them between each other, of which the most common is the downrange velocity measurement. The initial velocity of the projectile is measured and then the velocity is measured again at given time interval or distance from the muzzle. The best tool for this measurement is the Doppler radar. Optical chronograph can be used as well but with greater difficulty. Using the initial velocity, among other variables, the estimated velocities at a given time interval or distance are then computed by the ballistic solver and the results compared with the radar measurements.

7.1 Definition of fundamental variables

C_x $[-]$ – Measured drag coefficient of the projectile

C_s $[-]$ – Drag coefficient of the projectile corresponding to the given drag law

BC $[\text{lb} \cdot \text{in}^{-2}]$ – Ballistic coefficient of the projectile corresponding to the given drag law

i $[-]$ – Form factor corresponding to the given drag law

T_C $[°\text{C}]$ – Air temperature

h $[\text{m}]$ – Height above the se level

v_x $[\text{m} \cdot \text{s}^{-1}]$ – Projectile velocity at given distance x

n $[-]$ – Number of velocity measurements

S $[\text{m}]$ – Distance from the muzzle

d $[\text{m}]$ – Diameter of the projectile

m $[\text{kg}]$ – Weight of the projectile

7.2 Determination of ballistic coefficients

First, we need to compute the value of ballistic coefficients for each drag law. Since the G1 drag law is not accurately representing the shape of the JSB Exact projectile (pellet), the value of computed ballistic coefficient changes depending on the Mach number. Thus, we need to estimate the correct velocity around which the projectile is fired most often. Regarding 4.5 mm airgun projectiles the most common value of initial velocity is around $v_0 \approx 240 \, \text{m} \cdot \text{s}^{-1}$ ($v_{0\,Ma} \approx 0.71 \, \text{Ma}$).

Obtaining the drag coefficients for each drag law at velocity $v_{Ma} = 0.71$ Ma [7]:

$$C_s(0.71 \text{ Ma}, JSBE) = C_x(0.71 \text{ Ma}, measured) = 0.465,$$

$$C_s(0.71 \text{ Ma}, G1) = 0.217, \qquad C_s(0.71 \text{ Ma}, PRODAS \ V3) = 0.349.$$

Computing the value of ballistic coefficients (44):

$$BC(G1) = \frac{m \cdot C_s(G1)}{d^2 \cdot C_x} = \frac{0.000547 \cdot 0.217}{0.00452^2 \cdot 0.465} \cdot 0.00142233 = 0.0178 \text{ lb} \cdot \text{in}^{-2},$$

$$BC(JSBE) = \frac{m \cdot C_s(JSBE)}{d^2 \cdot C_x} = \frac{m}{d^2} = \frac{0.000547}{0.00452^2} \cdot 0.00142233 = 0.0381 \text{ lb} \cdot \text{in}^{-2},$$

$$BC(PRODAS \ V3) = \frac{m \cdot C_s(PRODAS \ V3)}{d^2 \cdot C_x} = \frac{0.000547 \cdot 0.349}{0.00452^2 \cdot 0.465} \cdot 0.00142233,$$

$$BC(PRODAS \ V3) = 0.0286 \text{ lb} \cdot \text{in}^{-2}.$$

As an initial comparison, we can also add the comparison of the JSB Exact projectile to the reference projectile using the form factor (42):

$$i(JSBE) = \frac{C_x}{C_s(JSBE)} = \frac{0.465}{0.465} = 1.00,$$

$$i(PRODAS \ V3) = \frac{C_x}{C_s(PRODAS \ V3)} = \frac{0.465}{0.349} = 1.33,$$

$$i(G1) = \frac{C_x}{C_s(G1)} = \frac{0.465}{0.217} = 2.14.$$

7.3   Comparison between ballistic solver computation and radar measurements

To verify and compare the accuracy of the JSBE drag law with the G1 drag law and the PRODAS V3 drag law approximation I used the JSB Exact projectile downrange velocity data measured by company JSB Match Diabolo using the amateur Doppler radar Labradar (Table 9). Note that the velocities are marked as $v_{S \ avg}$ where S is the instantaneous distance of the projectile from the muzzle. The measurements took place during following atmospheric conditions:

$$h = 204 \text{ m}, \qquad T_C = 16.7 \text{ °C}.$$

n	$v_{0\,avg}$	$v_{10\,avg}$	$v_{20\,avg}$	$v_{30\,avg}$	$v_{40\,avg}$	$v_{50\,avg}$
$[-]$	$[\mathrm{m\cdot s^{-1}}]$	$[\mathrm{m\cdot s^{-1}}]$	$[\mathrm{m\cdot s^{-1}}]$	$[\mathrm{m\cdot s^{-1}}]$	$[\mathrm{m\cdot s^{-1}}]$	$[\mathrm{m\cdot s^{-1}}]$
16	327.2	291.3	261.5	239.8	225.2	219.3
38	302.7	272.8	247.7	228.8	214.3	205.7
16	266.9	245.4	226.8	212.4	198.2	192.0
20	237.1	222.1	208.2	194.4	182.4	178.3
14	206.1	194.7	182.4	169.0	155.8	145.0
17	157.0	146.4	134.4	121.5	113.9	111.2

Table 9: Arithmetic means of measured velocities of the JSB Exact projectile with increasing distance from the muzzle. The first column expresses the total number of measurements from which the average was computed. The data were measured by JSB Match Diabolo company in Bohumín using a civilian Doppler radar Labradar.

The computation of downrange velocities based on JSB Match Diabolo initial velocity measurements was done by the ballistics solver B4E [9] using drag laws G1, JSBE and PRODAS V3 drag law approximation. The results were then separately compared to the radar measurement and after that to each other. Given that we have enough radar measurements we will be able to achieve quantitative comparison. All three drag laws were programmed into the B4E software [9], and we will refer to them through the computed ballistic coefficients.

v_0	v_{10}	v_{20}	v_{30}	v_{40}	v_{50}
$[\mathrm{m\cdot s^{-1}}]$	$[\mathrm{m\cdot s^{-1}}]$	$[\mathrm{m\cdot s^{-1}}]$	$[\mathrm{m\cdot s^{-1}}]$	$[\mathrm{m\cdot s^{-1}}]$	$[\mathrm{m\cdot s^{-1}}]$
327	288	261	239	222	205
303	272	249	229	212	196
267	244	226	209	193	179
237	219	203	188	174	161
206	191	177	163	151	139
157	145	134	124	114	106

Table 10: Velocities of the JSB Exact projectile (pellet) at given distances computed by the ballistic software B4E [9] using the G1 drag law [7].

v_0 [m·s^{-1}]	v_{10} [m·s^{-1}]	v_{20} [m·s^{-1}]	v_{30} [m·s^{-1}]	v_{40} [m·s^{-1}]	v_{50} [m·s^{-1}]
327	288	259	238	221	207
303	270	246	227	213	201
267	243	225	211	200	189
237	220	207	196	187	180
206	196	186	179	172	166
157	151	145	140	133	126

Table 11: Velocities of the JSB Exact projectile (pellet) at given distances computed by the ballistic software B4E [9] using the JSBE drag law (Table 8).

v_0 [m·s^{-1}]	v_{10} [m·s^{-1}]	v_{20} [m·s^{-1}]	v_{30} [m·s^{-1}]	v_{40} [m·s^{-1}]	v_{50} [m·s^{-1}]
327	287	260	239	221	204
303	271	248	229	211	196
267	245	226	208	193	179
237	219	202	188	174	161
206	191	177	164	152	141
157	146	135	125	116	108

Table 12: Velocities of the JSB Exact projectile (pellet) at given distances computed by the ballistic software B4E [9] using the PRODAS V3 drag law approximation (Table 6).

We can compare the drag laws by subtracting the computed velocities (Table 10, Table 11, Table 12) from the measured velocities (Table 9). Obtained difference between measured and computed data will be marked as Δv ($\Delta v = v_{computed} - v_{measured}$). The difference in velocities Δv displayed in Figure 23 is simultaneously the ultimate accuracy test and comparison of each drag law´s performance.
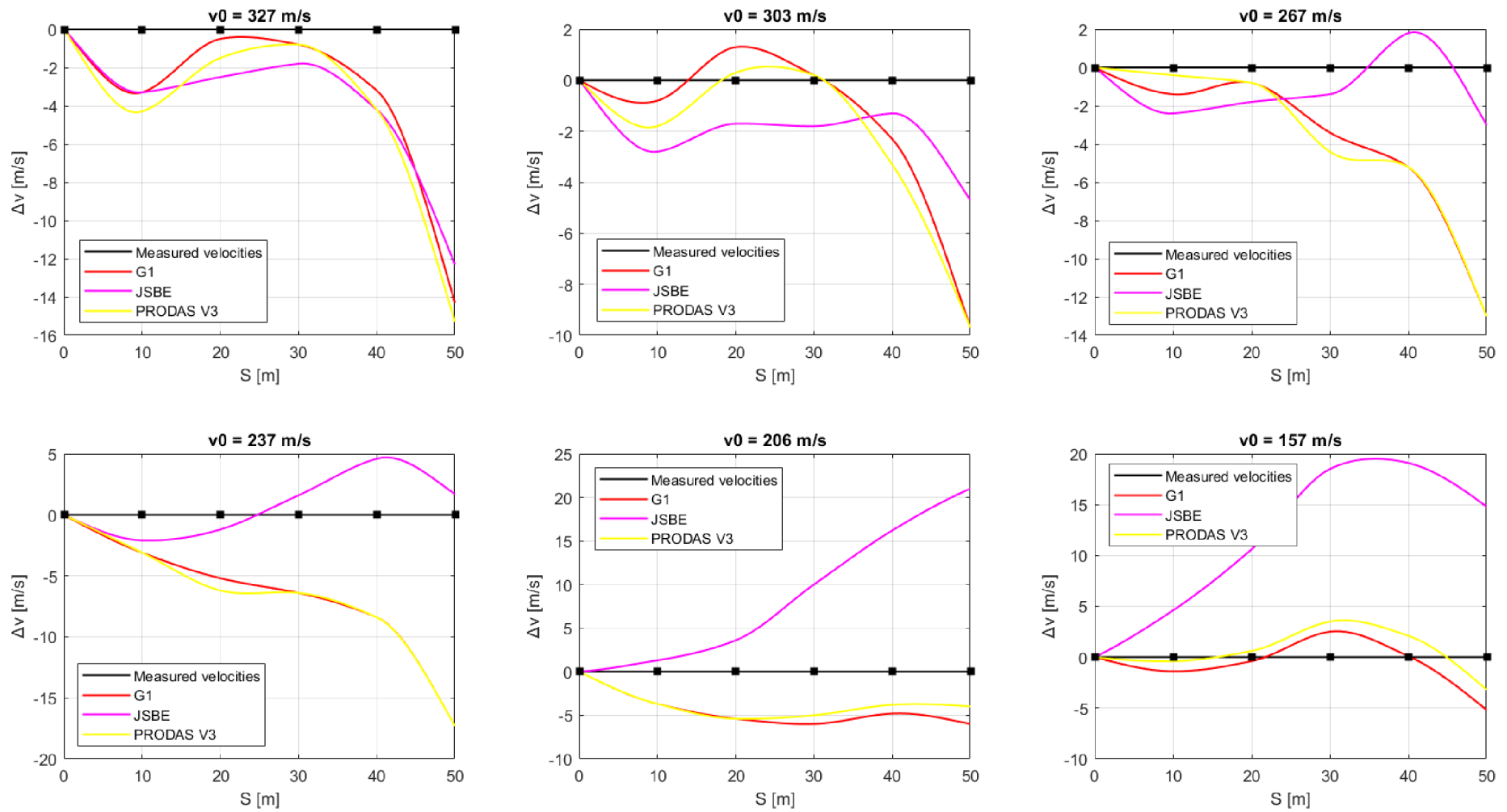
Figure 23: The differences between computed (red, purple, and yellow) and measured (black) velocities of the JSB Exact projectile (pellet). Segments are divided by projectile´s initial velocity v_0. The measured velocities (black) always assume zero deviations, because they serve as a reference. The colored plots correspond to the colored tables above (Table 9, Table 10, Table 11, Table 12).

To simplify the comparison, we will divide the results from the Figure 23 into two segments.

First segment: $v_0 = 327; 303; 267; 237 \text{ m} \cdot \text{s}^{-1}$. We can say that measured drag law JSBE outperformed both G1 and PRODAS V3 approximation. Also, PRODAS V3 approximation produced slightly better results than the G1 drag law.

Second segment: $v_0 = 206; 157 \text{ m} \cdot \text{s}^{-1}$. The JSBE drag law highly underperformed against both the G1 and PRODAS V3 approximation. Again, PRODAS V3 approximation was slightly more accurate than G1 drag law. The reason behind dividing the results in this way is the fact that the last two radar measurements are within the previously described region where the sudden decrease in drag coefficient has occurred. Due to the large deviation in results, we can conclude that the Labradar velocity measurement indirectly did not confirm the previously measured decrease in drag coefficient. This only strengthens the idea to thoroughly examine this region.

8 CONCLUSION

The contents of the thesis can be divided into two levels, theoretical and practical. The theoretical level was aimed to introduce the reader to basic concepts regarding solving ballistics trajectories using differential equations, numerical integration algorithms and the unusual behavior of the drag coefficient resulting in formation of drag laws. The dimensions of the JSB Exact 4.5 mm projectile had been defined and its aerodynamical properties approximated using software PRODAS V3. Furthermore, the measurement platform was described by a mathematical model resulting in the calculation of the drag coefficient from the measurements.

The practical level consists of recognition and evaluation of measurement errors, optimization of the measurement platform to yield usable data, and the measurement itself. Measurement evaluation resulted in formation of drag law JSBE referring to the projectile JSB Exact 4.5 mm. Drag law JSBE together with the drag law G1 and drag law approximation obtained using the PRODAS V3 were compared against the Doppler radar Labradar downrange velocity measurement provided by the company JSB Match Diabolo. Downrange velocity results corresponding to each drag law were computed using the B4E ballistic solver [9]. Performance of the final form of JSBE drag law is displayed in detail in Figure 23, which combines the Doppler radar experimental projectile velocity measurements against the computed projectile velocity based on the mentioned drag laws (JSBE, G1, PRODAS V3 Drag law approximation).

Overall, we can say that the drag law JSBE partially achieved desired results of improved accuracy compared to G1 drag law. During the measurement a critical problem in form of sudden decrease in drag was encountered which did not correspond to the Doppler radar measurements. PRODAS V3 drag approximation compared to G1 drag law achieved better accuracy in all scenarios and in the theoretical absence of JSBE, it would form a better substitution for the G1 drag law.

With all the above said, we can conclude that the goals of the work were met.

9 REFERENCES

[1] Agostino De Marco, Università degli Studi di Napoli Federico II, May 2020 ISA_Temperature – International Standard Atmosphere. In: Flight Mechanics for Pilots [online]. [cit. 26.1.2024]. Available from: https://agodemar.github.io/FlightMechanics4Pilots/mypages/international-standard-atmosphere/

[2] RBCN Meteorology data. In ČHMÚ [online]. Historical data of meteorology and climatology, January 2023 [cit. 10.3.2023]. Available from: https://www.chmi.cz/historicka-data/pocasi/denni-data/data-ze-stanic-site-RBCN

[3] Wikipedia contributors. Vapour pressure of water. In Wikipedia, The Free Encyclopedia [online]. January 2024, [cit. 28.1.2024], Available from https://en.wikipedia.org/w/index.php?title=Vapour_pressure_of_water&oldid=1193569527

[4] Wikipedia contributors. Speed of sound. In Wikipedia, The Free Encyclopedia [online]. January 2024, [cit. 28.1.2024]. Available from https://en.wikipedia.org/w/index.php?title=Speed_of_sound&oldid=1196750725

[5] Schaik, Wilhelm & Grooten, Mart & Wernaart, Twan & van der Geld, Cornelis. (2010). High Accuracy Acoustic Relative Humidity Measurement in Duct Flow with Air. Sensors (Basel, Switzerland) [online]. 10. 7421-33. 10.3390/s100807421. Available from: https://www.researchgate.net/figure/Speed-of-sound-vs-temperature-and-relative-humidity-according-to-2-p-1013-kPa-314_fig1_51873087

[6] Wikipedia contributors. List of Runge–Kutta methods. In Wikipedia, The Free Encyclopedia [online]. January 2024, [cit. 26.3.2024], Available from: https://en.wikipedia.org/wiki/List_of_Runge%E2%80%93Kutta_methods

[7] MCCOY, Robert. Modern exterior ballistics: the launch and flight dynamics of symmetric projectiles. Atglen, PA: Schiffer Publishing, 1999. ISBN: 0-7643-0720-7.

[8] ŠAPIRO, Jakov Matvejevič. Vnější balistika. Praha: Státní nakladatelství technické literatury, 1953. Řada strojírenské literatury.

[9] Tomáš Melichar, Software Ballistics for everyone 3.1 (B4E) [online]. November 2023 [cit. 30.1.2024]. Available from: https://ballistics4everyone.com/